# The influence of a rock glacier on the riverbed hydrological system

- Bastien Charonnat<sup>1,6,7</sup>, Michel Baraer<sup>1,6,7</sup>, Eole Valence<sup>2,6</sup>, Janie Masse-Dufresne<sup>1,6,7</sup>, Chloé Monty<sup>3</sup>,
- Kaiyuan Wang<sup>4</sup>, Elise Devoie<sup>5</sup>, Jeffrey M. McKenzie<sup>2</sup>
- <sup>1</sup>Hydrology, Climate and Climate Change laboratory École de technologie supérieure (ÉTS), Montreal, Quebec, Canada
- <sup>2</sup> Department of Earth and Planetary Science McGill University, Montreal, Ouebec, Canada
- <sup>3</sup> Department of Earth Sciences Simon Fraser University, Burnaby, British Columbia, Canada
- <sup>4</sup> Department of Earth, Environmental & Planetary Sciences Brown University, Providence, Rhode Island, United States 9
  - <sup>5</sup> Civil Engineering department Queen's University, Kingston, Ontario, Canada
  - <sup>6</sup> GEOTOP (Research Centre on the Dynamics of the Earth System), Montreal, Quebec, Canada
  - <sup>7</sup>CentrEau (Quebec Research Water Centre), Quebec City, Quebec, Canada
- 13 Correspondence to: Bastien Charonnat (bastien.charonnat.1@ens.etsmtl.ca)

# Abstract

10

11

12

14

17

18

19

21

22 23

26

- 15 Climate change is accelerating cryosphere degradation in mountainous regions, altering hydrological and geomorphological
- 16 dynamics in deglaciating catchments. Among cryospheric features, rock glaciers degrade more slowly than glaciers, providing
  - a sustained influence on water resources in alpine watersheds. This study investigates the role of a rock glacier interacting with
  - the Shár Shaw Tagà River (Grizzly Creek) riverbed in the St. Elias Mountains (Yukon, Canada), using a unique multimethod
  - approach that integrates hydro-physicochemical and isotopic characterization, drone-based thermal infrared (TIR) imagery,
- 20 and visible time-lapse (TL) imagery. Results assess that rock glaciers, due to their geomorphic properties, can constrict
  - riverbeds and alluvial aquifers, and control shallow groundwater flow, leading to notable changes in channel structure and
  - groundwater discharge. These disruptions promote downstream cryo-hydrological processes by facilitating aufeis formation
  - and modifying the physicochemical properties of streamflow. Additional findings highlight the critical role of rock glaciers
- 24 and proglacial systems in connecting mountain cryosphere and deep groundwater systems, with consequent implications for
- 25 mountain hydrology and water resources.

#### 1. Introduction

- 27 Climate change is profoundly transforming mountain regions, where the cryosphere plays a critical role in regulating water
- 28 resources essential for the sustainability of downstream ecosystems and communities. With rising global temperatures, high
- 29 mountain areas are experiencing accelerated deglaciation, characterized by glacial retreat and permafrost thaw (Hock et al.,
- 30 2019). These processes drive rapid geomorphological and hydrological reconfigurations in proglacial systems (Carrivick and
- 31 Heckmann, 2017). Understanding the impacts of cryosphere degradation on mountain hydrology and hydrogeology is essential

for predicting future water availability in these regions. Recently, the connectivity between the cryosphere and groundwater has been identified as a critical issue in mountain hydrology, directly influencing water resource sustainability under changing climatic conditions (van Tiel et al., 2024). In proglacial systems, riverbeds and outwash plains serve as critical hydrogeological components, sustaining baseflow and aquatic habitats (Käser and Hunkeler, 2016; Müller et al., 2024). However, the recharge and discharge dynamics of alluvial groundwater systems are intrinsically linked to upstream and adjacent cryospheric features (e.g., glaciers, seasonal snowpacks, etc.; Müller et al., 2024), as evidenced by aufeis formation. Aufeis, or icings, are layered ice formations that develop in winter when groundwater outflows persist under sub-zero temperatures for several months (Ensom et al., 2020). These formations can occur due to upwellings of groundwater encountering impermeable permafrost (Terry et al., 2020), with channel constriction further promoting their formation (Wainstein et al., 2014; Liu et al., 2021). In mountain environments, aufeis formations are common in outwash plains and are generally supplied by groundwater and meltwater from surrounding cryospheric sources (Chesnokova et al., 2020; Mallinson et al., 2019; Wainstein et al., 2014). Among cryospheric features, rock glaciers degrade more slowly than glaciers, allowing them to exert a prolonged influence on hydrological processes as glaciers retreat (Bolch and Marchenko, 2009; Harrison et al., 2021; Jones et al., 2021). Despite growing recognition of their hydrological importance, rock glaciers remain understudied compared to glaciers, particularly concerning their roles in deglaciating catchments (Jones et al., 2019). Rock glaciers are tongue-shaped landforms composed of rocky debris and ice, which creep due to the plastic deformation of the ice-debris matrix, concentrated in the shear horizon (Arenson et al., 2002)ir frozen content. They are commonly found in high mountain environments and occur in both discontinuous and continuous permafrost zones (Barsch, 1996). While existing studies primarily focus on the internal hydrological behavior of rock glaciers, research addressing their broader catchment-scale implications remains limited (Jones et al., 2019). Rock glaciers have been shown to buffer surface waters throughout the year, sustaining baseflow during dry periods and attenuating discharge response to intense precipitation events due to their internal structure (Bearzot et al., 2023; Reato et al., 2022; Wagner et al., 2021). Their hydrological behaviour is closely tied to the distribution of frozen and liquid water within them (Harrington et al., 2018; Wagner et al., 2016; Winkler et al., 2016). Unfrozen layers in summer can act as reservoirs and conduits for water flow (Halla et al., 2021; Harrington et al., 2018; Navarro et al., 2023; Wagner et al., 2020). In addition to liquid water, intact rock glaciers (i.e., containing frozen content) store significant volumes of solid water as interstitial or massive ice (Chakravarthi et al., 2022; Halla et al., 2021; Jones et al., 2018; Wagner et al., 2021). However, internal ice melt typically contributes only minimally to total rock glacier discharge (Arenson et al., 2022). In addition to modulating discharge, rock glaciers influence downstream water quality by increasing solute concentrations (Colombo et al., 2018; Colombo et al., 2019; Schreder et al., 2023; Engel et al., 2019; Wanner et al., 2023; Zarroca et al., 2021) and cooling stream temperatures

32

33

34

35

36

37

38

39

40 41

42

43

44

45

46 47

48

49

50

51

52

53

54

55

56

57

58

59

60

61 62

63

(Bearzot et al., 2023; Brighenti et al., 2019; Colombo et al., 2020). The physicochemical impact of rock glacier outflows is

particularly pronounced at the catchment scale when compared to catchments lacking glacial or periglacial landforms (Brighenti et al., 2023; Clow et al., 2021; Del Siro et al., 2023; Gammons et al., 2021; Robinson et al., 2022).

While much of the literature focuses on the downstream effects of rock glacier outflows (e.g., Brighenti et al., 2023; Robinson et al., 2022; Wagner et al., 2016; Wagner et al., 2021), their influence on the hydrogeomorphology of riverbeds and outwash plains remains understudied. Rock glaciers can advance, constrain, and dam riverbeds, potentially forming ponds, as reported in High Asia (Blöthe et al., 2019; Falatkova et al., 2020; Hewitt, 2014) and the Alps (Colombo et al., 2020). Furthermore, topographic changes driven by glacial retreat and paraglacial processes can force channel confinement (Marren and Toomath, 2014). Climate change has intensified rock glacier movement (Delaloye et al., 2010; Kummert et al., 2019; PERMOS, 2019), sometimes causing destabilization (Marcer et al., 2021) and channel disruption (Sorg et al., 2015). Additionally, sudden mass movements, such as the catastrophic collapse of rock glacier lobes, have triggered debris flows with downstream geomorphic impacts (Bodin et al., 2015; Scotti et al., 2017). The hydrological and geomorphic disturbances caused by advancing rock glaciers in valley systems are particularly notable, given the critical role of riverbeds and outwash plains in sustaining water resources. Despite recent studies (e.g., Falatkova et al., 2020; Wagner et al., 2021), research on the interactions between rock glaciers, the adjacent cryosphere, surface waters, and groundwater flow within valley systems is still underexplored.

- This study examines the influence of rock glaciers on surface and shallow groundwater flow within alpine riverbed hydrological systems. Specifically, it focuses on characterizing water fluxes in a section of the Shár Shaw Tagà catchment (St. Elias Mountains, Yukon, Canada) that is constrained by a rock glacier. We hypothesize that the rock glacier modulates interactions between surface water and shallow groundwater, thereby affecting the overall functioning of the riverbed system.

  To investigate these interactions, we employed a multimethod approach that was progressively refined as our observations and understanding of the system evolved:
  - We hypothesized that the rock glacier influences the formation of aufeis on the downstream outwash plain. To test
    this, we used time-lapse camera monitoring to track the development of aufeis and to identify the location and timing
    of winter outflows.
  - 2) Given the rock glacier's position at the outlet of a subcatchment and the lack of significant surface outflow, we hypothesized that it drains the subcatchment and contributes to river discharge via groundwater exfiltration. To assess this, we conducted a spring inventory, followed by a physico-hydrochemical characterization of springs and streams across the subcatchment. This allowed us to trace water sources and evaluate the rock glacier's influence on stream composition.
  - 3) Building on the previous findings, we hypothesized that a specific section of the riverbed serves as a major zone of groundwater exfiltration. To identify and map these zones, we conducted drone-based thermal infrared (TIR) surveys, enabling us to delineate areas of groundwater emergence and assess their spatial extent and relative magnitude.
  - The novelty of this research lies in its focus on the indirect hydrological impacts of a rock glacier—particularly in the absence of a visible, well-defined outflow. By integrating hydrological, hydrogeological, and geochemical methods, this study

advances our understanding of the complex role rock glaciers play in alpine watershed dynamics, and provides insights with
 broader applicability to similar environments worldwide.

This study investigates the influence of rock glaciers on surface and shallow groundwater flow within riverbed hydrological

systems. Specifically, it examines the critical impact of a rock glacier in the Shár Shaw Tagà catchment (St. Elias Mountains, Yukon, Canada) on the watershed's hydrological dynamics. The study's originality lies in its focus on the indirect effects of the rock glacier on the riverbed hydrological system, even in the absence of a prominent visible outflow. By providing insights into the hydrological, hydrogeological, and physicochemical processes associated with rock glaciers, this research offers findings that are globally applicable. A multimethod approach is employed, combining hydro-physicochemical and isotopic characterization, with synoptic sampling, drone-based thermal infrared (TIR) imagery, and visible time lapse (TL) imagery.

# 2. Study site

Shár Shaw Tagà, meaning Grizzly Creek in the Southern Tutchone indigenous language, is a 32 km² glacierized catchment located within the traditional lands of the Kluane First Nation and the White River First Nation (Fig. 1a). It also lies within the boundaries of Kluane National Park and Reserve in the St. Elias Mountains, southwestern Yukon Territory, Canada (61°05'132.6" N, 139°07'187.6" W). The eastern flank of the St. Elias Mountains experiences a dry subarctic climate, characterized by annual precipitation ranging from 300 to 500 mm yr¹ and a mean annual temperature between –8 °C and – 12 °C (Wahl et al., 1987). The eastern flank of the St. Elias Mountains experiences a dry subarctic climate, with annual precipitation ranging from 300 to 500 mm yr¹ (Wahl et al., 1987).

The upper Shár Shaw Tagà catchment (Fig. 1b) contains eight glaciers, the largest of which is G-A1, covering an area of 3.2 km². Faults are inferred along the valley floor (Dodds and Campbell, 1992). Due to its heavily fractured bedrock lithology and steep slopes, the valley is characterized by significant mass wasting processes and depositional features, including nine previously identified rock glaciers (Johnson, 1978; Evin et al., 1997). Between 1974 and 1997, Johnson participated to a series of geomorphological studies on the valley (Johnson, 1974; 1978; 1980; 1983; 1986; 1992; Evin et al., 1997), providing detailed descriptions of its landforms. The geomorphological identification and landform naming for these features, as established in Johnson's works, are adopted in this study to characterize the geomorphological setting.

The significance of ground ice landforms in the valley has prompted recent investigations, including a study on buried ice detection using ground-penetrating radar (GPR) in rocky and steep terrains (Tjoelker et al., 2024). Publications prior to 2024 referred to the area by the toponym "Grizzly Creek" rather than Shár Shaw Tagà. Of the nine rock glaciers identified by Johnson and Evin et al. (1978; 1997), seven extend into the riverbed along the valley floor, with some exerting considerable geomorphological constraints on the stream.

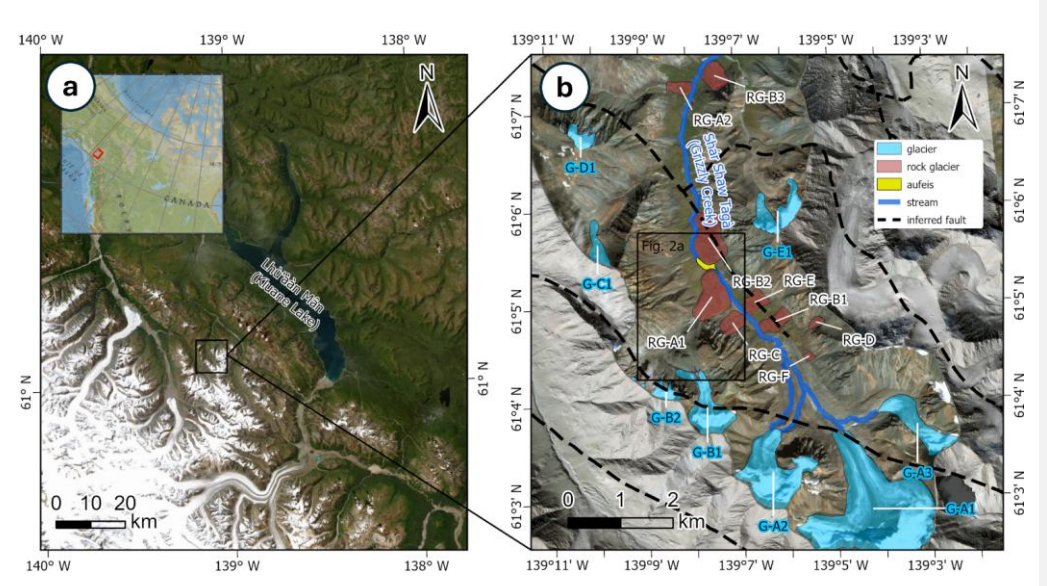


Fig. 1: (a) Overview map showing the location of the Shár Shaw Tagà valley in southwestern Yukon, Canada. (b) Enlarged view of the study area from panel (a), highlighting key geomorphological features. The black frame outlines the extent of the map shown in Fig. 2a. ArcticDEM data: Polar Geospatial Center (Porter et al., 2023). Basemap credits: Esri, Fig. 1: (a) Overview map showing the location of the Shár Shaw Tagà valley in southwestern Yukon, Canada. (b) Enlarged view of the study area from panel (a), highlighting key geomorphological features. The black frame outlines the extent of the map shown in Fig. 2b. Rock glaciers identified in earlier studies (Johnson, 1978; Evin et al., 1997) are marked in red. The study focuses on the RG-A1 rock glacier, located at the confluence of the G-A1 and G-B1 subcatchments. The Shár Shaw Tagà River, fed by glaciers G-A1, G-A2, and G-A3, is constrained against the opposite talus slope by the RG-A1 rock glacier. An aufeis formation, highlighted in yellow, develops during winter on the outwash plain between RG-A1 and RG-B2. The fault network inferred by Dodds and Campbell (1992) reveals the area's fractured bedrock and faulted geology. ArcticDEM data: Polar Geospatial Center (Porter et al., 2023). Basemap credits: Esri.

The present study investigates the hydrological influence of the RG-A1 rock glacier, located on the western side of the upper Shár Shaw Tagà valley. RG-A1, first identified by Johnson (1978), spans elevations between 1700 and 1850 m a.s.l. The southern lobes of RG-A1 appear older, characterized by vegetation cover and a smoother frontal morphology, while the northern lobes are younger, with sparse or absent vegetation, sharper forms, and a steeper front (Johnson, 1978). A frozen layer, 20 to 40 m thick was detected in RG-A1 during a previous geophysical study, which also suggested the presence of massive ice lenses at depth (Evin et al., 1997). The front of RG-A1 advances in the valley, constraining the Shár Shaw Tagà

River against the opposing talus slope. Although previous studies did not classify the opposing talus slope as a rock glacier, it is suspected to be a protalus rampart (or small active rock glacier) based on environmental and topographic criteria outlined in Scapozza (2015), such as the absence of an upstream permanent snow field, the presence of coarse boulders in the upslope area, a steep front with exposed fine sediments, and its juxtaposition and superimposition to other rock glaciers. The outwash plains upstream and downstream of RG-A1 are separated by a "narrow section" of the Shár Shaw Tagà River, which can be divided into two subsections: N1 and N2 (Fig. 2). N1 extends from the outlet of the upstream outwash plain to a bedrock outcrop visible on the opposite talus slope to RG-A1. N2 extends from this bedrock outcrop to the outlet of the "narrow section", where the rivers enters the downstream outwash plain. An aufeis forms in winter in the downstream outwash plain, as confirmed through field studies since 2018 and satellite imagery. No aufeis has been detected in the upstream outwash plain

during this period.

In 1974, Johnson (1978) observed that meltwater drained into a sinkhole located in the rooting zone of RG-A1 (at approximately 1850 m a.s.l.), with no major resurgence observed at the front (at 1700 m a.s.l.). In 1975, a new sinkhole was observed upstream of the first one, and a significant resurgence was reported on the northern part of RG-A1. Dry channels on the surface of RG-A1 in 1975 were interpreted by Johnson as abandoned surface drainage pathways, highlighting the dynamic and variable hydrological behaviour of RG-A1.

Field observations by our research team from 2018 to 2023 confirm the absence of a significant visible outlet from the rock

glacier, despite its location downstream of a 8 km<sup>2</sup> subcatchment, consisting of the G-B1 and G-B2 glaciers. The only visible outlets consist of low-discharge springs around the RG-A1 front, particularly concentrated along the N1 subsection. During low-discharge periods such as June 2023, we observed that the water from the Shár Shaw Tagà River infiltrates the riverbed, leaving it dry before entering the outwash plain upstream of RG-A1. However, water was observed to flow again within the riverbed in the N1 subsection, visually sustained by springs and seepage. During high-flow periods, the springs emerge directly under the front of RG-A1. In dry periods, like June 2023, the springs shift away from the front and align with the current river level, 10 to 20 m downstream.

#### 3. Methods

#### 3.1 Method overview

Since 2018, we have been investigating the hydrological and hydrochemical influence of RG-A1 on the Shár Shaw Tagà catchment using a multimethod approach. Our primary hypothesis posits that RG-A1 influences the formation of aufeis in the downstream outwash plain. To test this hypothesis, we monitored aufeis formation and winter outflows by deploying a timelapse (TL) camera in 2018, followed by a second TL camera installation in 2019. Additionally, an inventory of springs was conducted in 2018, 2019 and 2021. These initial observations provided a preliminary understanding of the location and timing of cryo-hydrological processes in the vicinity of RG-A1.

Given the position of RG-A1 at the outlet of G-B1 subcatchment and the absence of significant surface outflow from it, we hypothesized that the rock glacier drains the G-B1 subcatchment, and contributes to river discharge through groundwater exfiltration. To investigate this, we sampled the Shár Shaw Tagà River and springs near RG-A1 in 2022 and 2023 to analyze their physicochemical properties. Sampling was extended to the entire subcatchment upstream of RG-A1, including the ice-debris complex and the G-B1 glacier snout, to identify potential water sources contributing to RG-A1's groundwater outflow. The aim of this analysis was to elucidate the origins of the spring waters and assess their hydrochemical impact on the Shár Shaw Tagà River.

The final phase of the study focused on characterizing the extent and magnitude of groundwater-surface interactions underlined by the spring inventory and hydrochemical analysis. Due to the large spatial scale (several hundred meters) and the challenges associated with differential stream gauging in proglacial environments, stream temperature heterogeneity was selected as a proxy for detecting groundwater exfiltration (Baker et al., 2018; Brunner et al., 2017; Kalbus et al., 2006; Webb et al., 2008). To this end, a drone-based thermal infrared (TIR) survey was conducted in June 2024 to identify zones of groundwater exfiltration. This survey provided a detailed map of preferential groundwater exfiltration locations, contributing to the overall

#### 3.12 TL monitoring

Two RGB timelapse (TL) cameras, designated TL1 and TL2, were positioned above the right bank of the Shár Shaw Tagà River (61°5′26" N, 139°7′34" W; -(Fig. 2). TL1 was installed in 2018, focused on the central area of the outwash plain immediately downstream of RG-A1. In 2019, TL2 was added adjacent to TL1, extending its field of view from the upper margin of TL1's coverage to the outlet of the N2 subsection of the Shár Shaw Tagà River. Both cameras were configured to capture four images daily at 8:00, 11:00, 13:00, and 16:00. The visual analysis of the images captured by the TL cameras involved identifying signs of surface overflow on the developing aufeis and documenting the occurrence of such events throughout the winter, following the protocol outlined by Chesnokova et al. (2020).

#### 3.23 Physico-hydrochemical characterisation

understanding of the rock glacier's influence on the riverbed hydrologic system.

### 3.23.1 Sampling and field measurements

Physico-hydrochemical characterisation was undertaken over three distinct campaigns: June 2022, August 2022, and June 2023. These campaigns targeted both the Shár Shaw Tagà River and springs inventoried from 2018 to 2021, capturing different hydrological conditions. The June 2022 campaign coincided with the melt of a late and substantial snowpack. The August 2022 campaign took place during late summer, when glacial ablation was at its peak. The June 2023 campaign was conducted following a winter with reduced snowpack and early snowmelt, after the primary snowmelt phase but before summer glacial ablation commenced, while glaciers remained snow-covered.

Field measurements included in situ pH, electrical conductivity (EC, corrected to 25 °C, expressed in μS cm<sup>-1</sup>), and water temperature (°C). Water samples were collected for laboratory analyses. Additionally, in June 2023, in situ radon measurements were performed to further investigate groundwater contributions. Measurements were taken at each sampling site using a calibrated Hanna HI 98195 multiparameter meter. Water sampling followed a synoptic approach for cycles of 1-2 days, avoiding precipitation periods (e.g. Baraer et al., 2009). When possible, sites were sampled multiple times within each campaign to account for diurnal fluctuations in physicochemical parameters. Samples were categorized into four types (Table A1): glacial outlets from the RG-B1 snout (S-GL#), streams in the ice-debris complex located between the RG-B1 snout and RG-A1 (S-IDC#), springs at the RG-A1 front and opposite talus (S-RG#), and Shár Shaw Tagà River (S-R#). Water samples were filtered using 0.45 µm syringe filters and collected in 50 mL HDPE bottles, rinsed three times prior to sampling. Not all sites were accessible during each campaign (Table A1), due to factors such as no flow or safety concerns related to snow cover and rockfalls. Results were analyzed following the methodology of Baraer et al. (2015). Samples for major ion analysis were stored in a dark environment at 4 °C until analysis. Major ions (Ca<sup>2+</sup>, Mg<sup>2+</sup>, Na<sup>+</sup>, Cl<sup>-</sup>, SO<sub>4</sub><sup>2-</sup>) and minor ions (K<sup>+</sup>, F<sup>+</sup>) were analyzed at the LG2 laboratory, École de technologie supérieure (ÉTS), Montreal, Canada. Cation concentrations were determined using an inductively coupled plasma optical emission spectrometer (5110 ICP-OES, Agilent), and anion concentrations were measured with an ion chromatograph (Dionex ED50, Thermo Fisher Scientific). Bicarbonate (HCO<sub>3</sub><sup>-</sup>) concentrations were calculated from the charge balance equation, and total dissolved solids (TDS) were derived from the sum of ion concentrations. Stable isotopic composition of the water molecule ( $\delta^{18}$ O and  $\delta^{2}$ H) was measured using a cavity ringdown spectrometer (Picarro L2130-i) at the LG2 laboratory (ÉTS), Montreal, Canada, expressed in % relative to Vienna Standard Mean Ocean Water (VSMOW). Internal reference waters were used for normalization after every 3 injections. The analytical uncertainty is  $\pm 0.13$ % for  $\delta^{18}O$  and  $\pm 1.5$  % for  $\delta^{2}H$ . The nearest local meteoric water line (LMWL) is established for the Whitehorse area 220 km east of Shár Shaw Tagà (Birks et al., 2004). The LMWL is similar to isotopic compositions found in the Lhù'ààn Mân' (Kluane Lake), 25 km east of Shar Shaw Tagà (Brahney et al., 2010). The LMWL is displayed alongside the analyses results as reference (Fig. 6d, Fig. 7d and Fig. 8d) but we prefer not to assume direct applicability to our data. The LMWL is displayed alongside the analyses results as reference (Fig. 6d, Fig. 7d and Fig. 8d). Radon (222Rn) serves as a natural tracer to detect groundwater exfiltration in streams (Cartwright and Hofmann, 2016). In situ radon activities were measured at four locations in the N1 subsection, including S-RG8 and S-RG9A springs, and at the upstream and downstream ends of the N1 subsection (S-RUP and S-R1, respectively). A portable RAD7 Radon Monitor (Durridge) was used, coupled with the Rad Aqua accessory (Durridge) for radon degassing. Results are reported in Bq m<sup>-3</sup>, with an analytical uncertainty of  $\pm$  220 Bg m<sup>-3</sup>.

206

207

208

209

210

211

212

213

214

215

216

217

218219

220

221

222

223

224

225

226

227

228

229

230

231

232

233

234

235

# 3.23.2 Principal Component Analysis and clustering

- Principal Component Analysis (PCA) was employed to classify the origins of the sampled water and to identify sample groups that influence the chemistry of the Shár Shaw Tagà River. For each of the three sampling campaigns, PCA was performed using a set of independent variables: water temperature, δ<sup>18</sup>O, Na<sup>+</sup>, Mg<sup>2+</sup>, Ca<sup>2+</sup>, and SO4<sup>2-</sup>. These major ions were selected as they exhibited concentrations above the detection limit in more than 95 % of the samples. Principal components explaining at least 90 % of the total variance were retained for further analysis to ensure the robustness of the PCA.

  After conducting PCA, clustering analysis was performed using the k-means algorithm for each campaign (Lloyd, 1982;
- After conducting PCA, clustering analysis was performed using the k-means algorithm for each campaign (Lloyd, 1982; MacQueen, 1967). This analysis was based on the sample scores derived from the selected principal components. The maximum number of clusters was set at 25 % of the total number of samples for each campaign, which corresponded to 5, 9 and 7 for the campaigns of June 2022, August 2022, and June 2023, respectively. The algorithm determined the resulting clusters were by associating samples with dominant combinations of variables, thereby highlighting inherent patterns within the dataset.

# 3.34 TIR survey

Aerial and handheld thermal infrared (TIR) devices have been demonstrated as effective tools for mapping groundwater discharge into streams (Toran, 2019). Specifically, drone-based TIR technology allows for high spatial resolution observations of surface water—groundwater interactions (Vélez-Nicolás et al., 2021). Two common approaches for TIR surveys were considered: 1) generating stream temperature maps using high-definition TIR image orthomosaics from overlapping images (e.g., Abolt et al., 2018; Casas-Mulet et al., 2020; Rautio et al., 2015), and 2) using TIR videos or real-time scans (handheld or drone-based) to visualize mixing plumes and record GPS coordinates of observed points (e.g., Barclay et al., 2022; Briggs et al., 2016; Iwasaki et al., 2023).

While georeferenced thermal maps provide mesoscale coverage, they require stable flying conditions, ground control points, and extensive post-processing (Webb et al., 2008). In contrast, TIR video or live scans allow for real-time visualization of mixing dynamics in smaller-scale areas (Antonelli et al., 2017). Given our goal to identify and characterize groundwater exfiltration zones, we chose the TIR video approach. This method does not require precise absolute temperature but relies instead on relative contrasts between stream water and suspected groundwater inflows. Prior studies (Antonelli et al., 2017; Briggs et al., 2016; Iwasaki et al., 2023; Iwasaki et al., 2024) have shown that TIR video, even without embedded temperature scales, effectively highlights such contrasts.

Drone-based TIR video surveys were conducted on 28 June 2024, between 08:00 and 10:00, to maximize the coverage of shaded sections of the stream. The surveys were conducted using a DJI Mavic 3T Enterprise, equipped with a DJI RTK module and a DJI D-RTK 2 mobile station for GNSS base-station support. The Mavic 3T features a 48-megapixel RGB camera with a 24 mm focal length and a 640 × 512-pixel thermal camera with a 40 mm focal length. The drone was manually controlled to optimize the capture of surface temperatures across wide sections of the Shár Shaw Tagà River, recording both TIR and RGB

videos simultaneously. Flight altitudes ranged from 5 to 20 m above ground level, depending on the section. All flights were manually piloted at low altitudes and near-nadir angles to reduce geometric distortion and minimize emissivity-related error (Torgersen et al., 2001; Dugdale et al., 2016). The survey began approximately 180 m upstream of the N1 subsection and ended around 800 m downstream of the N2 subsection (Fig. 2). Due to difficulties in flying over the narrow section, it was surveyed twice at different elevations. The TIR video was visually analyzed to identify cold groundwater exfiltration areas using two criteria: 1) a clear contrast between the dominant stream surface temperature and the suspected exfiltration area, with an area larger than 10 cm<sup>2</sup>, and 2) the presence of a turbulent mixing zone at least 1 m in length immediately downstream of the suspected area (flight data and information are available as Supplemental Material in Charonnat and Baraer, 2025). Absolute temperatures were not derived due to the absence of a calibrated color scale in the TIR video; instead, detection relied on qualitative identification of relative temperature differences appearing as visual color contrasts in the TIR video—typically, colder areas appeared as blue-toned patches compared to the green-toned stream and red-toned sunlit boulders. When both criteria were met, the RGB video was used for confirmation. The Shár Shaw Tagà River, originating from glacial melt, has a substantial suspended sediment load, whereas groundwater is nearly free of suspended sediments. This contrast is visible in the RGB video frames. The observed thermal contrasts were consistent with previously measured field temperature differences between springs and stream water, typically >2°C and <6°C (Table S1), and exceeded the uncertainty range of uncorrected thermal imagery under field conditions (Zappa and Jessup, 1998). Finally, images of confirmed groundwater exfiltration areas were extracted from the videos for size evaluation. Exfiltration areas from the left bank were labeled TIR-L#, and those from the right bank were labeled TIR-R#. Aerial or handheld thermal infrared (TIR) devices have been demonstrated as effective tools for mapping groundwater discharge into streams (Toran, 2019). Specifically, drone-based TIR technology allows for high spatial resolution observations of surface water-groundwater interactions (Vélez-Nicolás et al., 2021). Two common approaches for TIR surveys were considered: 1) generating stream temperature maps using high-definition TIR image ortho-mosaics from overlapping images (e.g., Abolt et al., 2018; Casas-Mulet et al., 2020; Rautio et al., 2015), and 2) using TIR videos or real-time scans (handheld or drone-based) to visualize mixing plumes and record GPS coordinates of observed points (e.g., Barclay et al., 2022; Briggs et al., 2016; Iwasaki et al., 2023). While georeferenced thermal maps provide mesoscale coverage, they require stable flying conditions, ground control points, and extensive postprocessing (Webb et al., 2008). In contrast, TIR video or live scans allow for real-time visualization of mixing dynamics in smaller-scale areas (Antonelli et al., 2017). Given our goal to identify and characterize groundwater exfiltration zones, we chose the TIR video approach. Drone-based TIR video surveys were conducted on 28 June 2024, between 8:00 and 10:00, to maximize the coverage of shaded sections of the stream. The surveys were conducted using a DJI Mavic Enterprise 3T, equipped with a DJI RTK module and a DJI D-RTK 2 mobile station for GNSS base-station support. The Mavic 3T features a 48-megapixel RGB camera with a 24

269

270

271

272

273

274

275

276

277

278

279

280

281

282

283

284

285

286

287

288

289

290

291

292

293

294

295

296

297

298

299

300

301

mm focal length and a 640x512-pixel thermal camera with a 40 mm focal length. The drone was manually controlled to

optimize the capture of surface temperatures across wide sections of the Shár Shaw Tagà River, recording both TIR and RGB videos simultaneously. Flight altitudes ranged from 5 to 20 m, depending on the section.

The survey began 180 m upstream of the N1 subsection and ended 800 m downstream of the N2 subsection (Fig. 2). Due to difficulties in flying over the "narrow section", it was surveyed twice at different elevations.

The TIR video was visually analyzed to identify cold groundwater exfiltration areas using two criteria: 1) a clear contrast between the dominant stream surface temperature and the suspected exfiltration area, with an area larger than 10 cm², and 2) the presence of a turbulent mixing zone at least 1 meter in length immediately downstream of the suspected area (flight data and information are available as Supplemental Material in Charonnat and Baraer, 2025). When both criteria were met, the RGB video was used for confirmation. The Shár Shaw Tagà River, originating from glacial melt, has a substantial suspended sediment load, whereas groundwater is nearly free of suspended sediments. This contrast is visible in the RGB video frames. Finally, images of confirmed groundwater exfiltration areas were extracted from the videos for size evaluation. Exfiltration areas from the left bank were labeled TIR-L#, and those from the right bank were labeled TIR-R#.

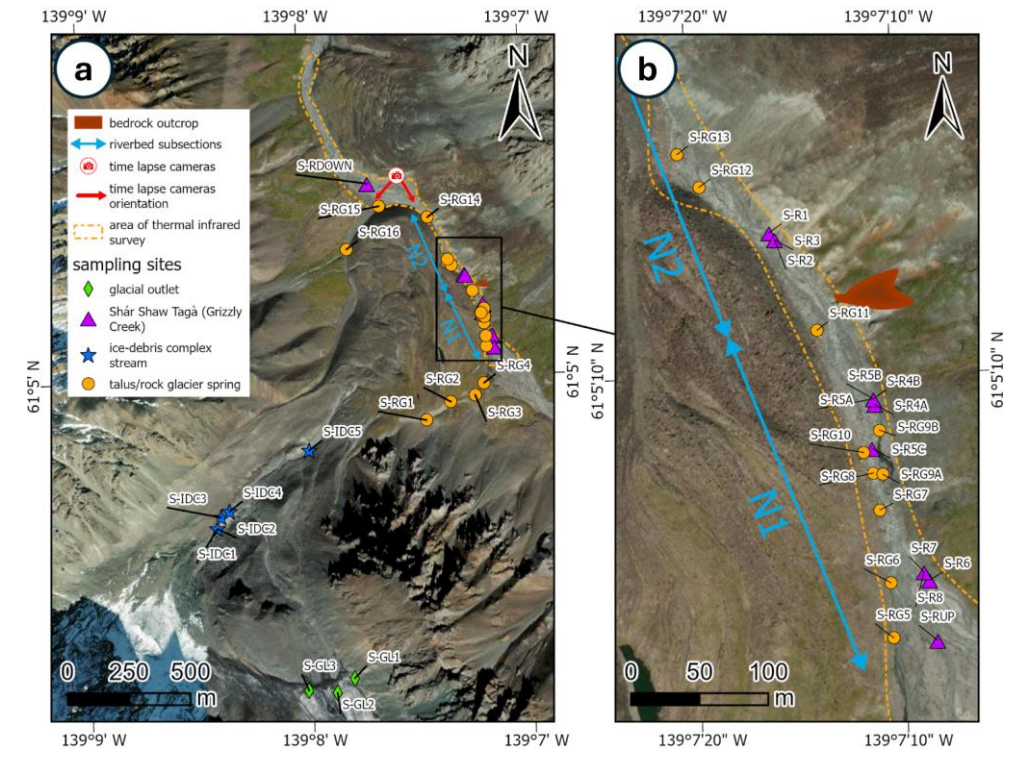


Fig. 2: Map illustrating the methods used in this study. Panel (a) corresponds to the area shown in Fig. 1b, while panel (b) provides a zoom-in of panel (a). A bedrock outcrop on the talus slope opposite to RG-A1 marks the division of the Shár Shaw Tagà River's "narrow section" into two subsections, N1 and N2, as shown on the map. The spring locations represent the outflow points observed during the August 2022 campaign, though their positions may vary depending on hydro-meteorological conditions. Basemap credits: Esri, Fig. 2: Map illustrating the methods used in this study. Panel (a) corresponds to the area shown in Fig. 1b, while panel (b) provides a zoom in of panel (a). A bedrock outcrop on the talus slope opposite to RG-A1 marks the division of the Shár Shaw Tagà River's "narrow section" into two subsections, N1 and N2, as shown on the map. The positions of time-lapse cameras TLC1 and TLC2 are indicated on the southern front of RG-B2, with their southwest and southeast orientations, respectively. The area covered by the drone based TIR survey extends along the Shár Shaw Tagà riverbed from the northern front of RG-B2 downstream to the southern front of RG-A1, passing through two outwash plains. Sampling sites are depicted with different symbols depending on their type: glacial outlet from the G-B1 snout (S-GL#), Shár Shaw Tagà River (S-R#), ice-debris complex stream (S-IDC#), and springs at RG-A1 front and opposite talus (S-RG#). The spring locations represent the outflow points observed during the August 2022 campaign, though their positions may vary depending on hydro-meteorological conditions. Basemap credits: Esri.

#### **4. Results**

#### 4.1 TL monitoring

Between 2018 and 2021, TL1 monitored aufeis formation during the winters of 2018-2019 and 2019-2020 (Fig. 3 and 4a). No aufeis formation was observed during the winter of 2020-2021. The onset of aufeis development varied between the two winters: in 2018-2019, it began in early November and continued to develop throughout the winter season, whereas in 2019-2020, it started in February and progressed through February and March (Fig. 3). The development of the aufeis in both winters occurred in phases characterized by multiple flood events. Visible ablation of the aufeis began in May, with complete melt

occurring by June in both 2019 and 2020. The aufeis that formed during the winters of 2018-2019 and 2019-2020 spanned the entire width of the river, from the RG-A1 front to the RG-B2 front.

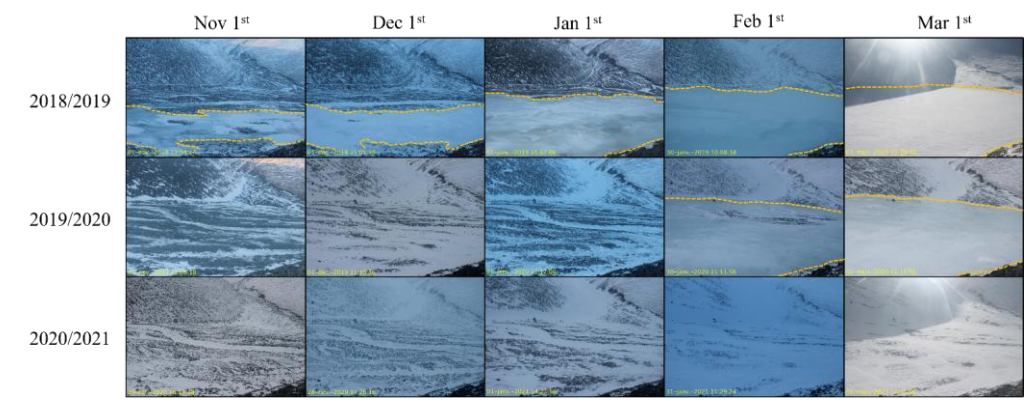
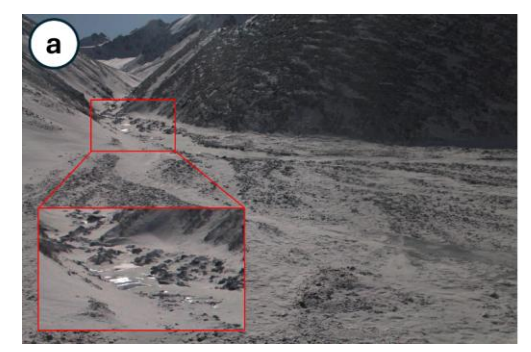


Fig. 3: Monthly timelapse images captured by TL1 of the aufeis from November 1st to March 1st during the winters of 2018-2019, 2019-2020, and 2020-2021. The yellow dashed line indicates the extent of the aufeis in each image when visible. The timelapse images were selected based on the closest date to the first day of each month, with consideration given to image quality. Note that no aufeis formation occurred during the 2020-2021 winter.

TL2, installed in 2019 next to TL1 and oriented upstream, recorded the formation of the aufeis in the winter of 2019-2020 and its absence during 2020-2021. In the winter of 2020, TL2 captured reflections of liquid water and/or ice at the end of the N2 subsection, when the river was dry (Fig. 4). In subsequent days, the aufeis was observed to form in the downstream outwash plain, starting from the end of the N2 subsection. This observation suggests that the overflowing water contributing to the formation of the aufeis originates from the "narrow section" of the Shár Shaw Tagà River.





- Fig. 4: Initiation of an aufeis in the downstream outwash plain, captured by TL2 on (a) 04/01/2020 at 08:00, and (b) 08/01/2020 at 11:00. The light in the raw images has been enhanced to improve picture quality. Both images are oriented towards the end of the N2 subsection and the entrance of the downstream outwash plain. (a) At 8:00 on 04/01/2020, the aufeis has not yet formed, but
- reflections of ice and/or liquid water are visible at the end of the N2 subsection, during a time when the Shár Shaw Tagà River is dry. (b) At 11:00 on 08/01/2020, the aufeis has started to form in the outwash plain, extending from the end of the N2 subsection.
- 356 The repetitive monitoring of the aufeis provides evidence of overflow events during late fall and winter, particularly in the
- 357 2018-2019 and 2019-2020 periods. The formation of the aufeis is attributed to groundwater outflow from the "narrow section"
  - of the Shár Shaw Tagà River, as the river runs dry in winter in the downstream outwash plain and no aufeis forms in the
- 359 upstream outwash plain. This finding aligns with the high density of springs inventoried along the N1 subsection.

# 4.2 Physico-hydrochemical characterization

#### 4.2.1 Sampling and field measurements

- A high concentration of springs was reported along the N1 subsection of the Shár Shaw Tagà River (S-RG5 to S-RG11) from
- 2018 to 2021, and during the 2022 sampling campaigns. This led to a dedicated sampling campaign in June 2023. Many of
- these springs were sampled across multiple campaigns, indicating their long-term flow. The June 2022 and August 2022
- 366 sampling campaigns can be directly compared for the springs at RG-A1's front, given their similar spatial coverage and
- 367 sampling sites. In contrast, the June 2023 sampling campaign focused specifically on the N1 subsection of the river (Table
- 368 A1).

358

360 361

362

363

364

365

371

376

- 369 The mean water temperature for samples collected from the springs at RG-A1's front in June 2022 was 0.90 °C, with a range
- of 3.16 °C, slightly colder than in samples from August 2022, exhibiting a mean temperature of 1.38 °C and a range of 3.77
  - °C (Table S12). While cold temperatures in June 2022 may have been strongly influenced by recent snowmelt, no snow
- 372 remained at the lower elevations of the catchment in August 2022. In late season, cold groundwater outflows (< 2 °C) suggest
- the possible presence of frozen content in the vicinity of springs (Carturan et al., 2016; Frauenfelder et al., 1998; Haeberli,
- 374 1975; Scapozza, 2009).
- 375 The June 2022 campaign recorded a lower mean EC in springs at RG-A1's front of 225.64 μS cm<sup>-1</sup>, with a range of 439.10 μS
  - cm<sup>-1</sup>, compared to 490.82 µS cm<sup>-1</sup> with a range of 546.72 µS cm<sup>-1</sup> in August 2022. These results indicate dilution due to
- 377 snowmelt in early season and increased groundwater contribution in late season, consistent with results from other rock glacier
- 378 hydrology studies (Jones et al., 2019). The high EC ranges highlight the heterogeneous behavior of the sampled springs. Mean
- 379 pH values were 8.47 in June 2022 and 8.13 in August 2022, with ranges of 1.84 and 1.00, respectively.
- 380 The mean isotopic composition was more depleted in the springs at RG-A1's front in June 2022 (-23.57 ‰ vs. VSMOW for
  - $\delta^{18}O$  and -183.69 % vs. VSMOW for  $\delta^{2}H$ , with ranges of 1.64 % and 8.78 %, respectively) compared to August 2022 (-21.01
- 382 %vs. VSMOW for δ18O and -169.20 %vs. VSMOW for δ2H, with ranges of 1.38 % and 9.68 %, respectively). This depletion
- 383 is associated with a higher snowmelt contribution in June 2022. Solute concentrations were generally lower in June 2022,
- 384 frequently falling below detection limits for chlorides (all samples < 0.13 mg L<sup>-1</sup>), potassium (13 out of 20 samples < 0.01 mg

 $L^{-1}$ ), sodium (13 out of 20 samples < 0.09 mg  $L^{-1}$ ), and magnesium (1 out of 20 samples < 0.03 mg  $L^{-1}$ ). In contrast, in August 2022, solute concentrations exceeded detection limits for 38 out of 39 samples for all elements except chlorides (36 out of 39 samples < 0.13 mg  $L^{-1}$ ).

The June 2023 campaign showed a mean water temperature for the rock glacier springs of  $1.40^{\circ}$ C, with a range of  $0.23^{\circ}$ C. The mean EC value for June 2023 was  $678.43~\mu$ S cm<sup>-1</sup>, with a range of  $172.00~\mu$ S cm<sup>-1</sup>. The mean pH value was 7.82 with a range of 0.23. The mean isotopic composition for the springs during this campaign was -22.86~% vs. VSMOW for  $\delta^{18}$ O and -178.11~% vs. VSMOW for  $\delta^{2}$ H, with ranges of 0.30~% and 1.10~%, respectively.

In June 2023, while the Shár Shaw Tagà River level was lower than in previous years for the same period,  $^{222}$ Rn activities were similar at S-RG8 and S-RG9A, ranging from  $10.17 \times 10^3 \pm 0.22 \times 10^3$  Bq m<sup>-3</sup> to  $10.85 \times 10^3 \pm 0.19 \times 10^3$  Bq m<sup>-3</sup> (Fig. 5). These springs are located along the N1 subsection of the river, at the left and the right of the stream, respectively. In contrast, the Shár Shaw Tagà River at the upstream end of the N1 subsection (S-RUP) exhibited low activities  $(0.36 \times 10^3 \pm 0.06 \times 10^3$  Bq m<sup>-3</sup>), while the downstream end of N1 (S-R1) showed significantly higher activities  $(5.46 \times 10^3 \pm 0.14 \times 10^3$  Bq m<sup>-3</sup>). These results indicate a major groundwater input to the Shár Shaw Tagà River in the N1 subsection, where S-RG8 and S-RG9A are located.

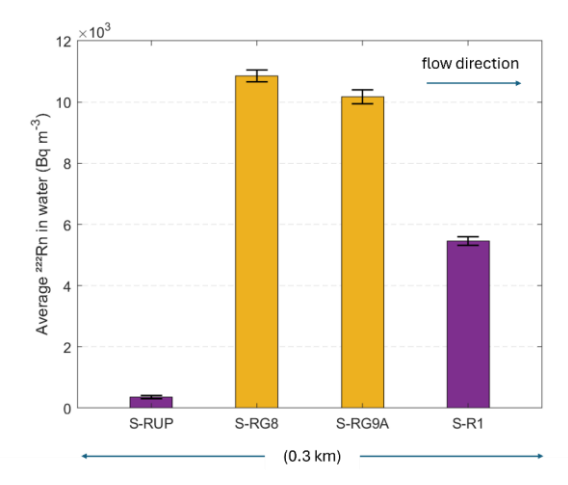


Fig. 5: 222Rn activities measured with a portable RAD7 Radon Monitor (Durridge) in June 2023. Data were collected at springs S-RG8 and S-RG9A (orange) and along the Shár Shaw Tagà river at upstream (S-RUP) and downstream (S-R1) sites (purple). The bars are arranged from left to right in spatial sequence from upstream to downstream. The error bars represent the uncertainties in the radon activity measurements.

# 4.2.2 Principal Component Analysis and clustering

#### Samples collected in June 2022

 Principal Component (PC) 1 accounts for 60.96 % of the variance in the dataset and primarily reflects the influence of mineral elements, with PC scores ranging from 0.47 to 0.50 (Fig. 6a). PC2 and PC3, explaining 18.29 % and 14.10 % of the variance, respectively, exhibit contrasting associations with the  $\delta^{18}$ O ratio and temperature. PC2 displays a strong positive correlation with the  $\delta^{18}$ O ratio (0.73) and a negative correlation with temperature (-0.67), whereas PC3 shows positive correlations with  $\delta^{18}$ O (0.62) and temperature (0.71).

Clustering analysis based on PCA reveals two distinct clusters among the June 2022 samples (Fig. 6b). Cluster 1 comprises 17 samples characterized by low concentrations of mineral elements (Fig. 6c), with total dissolved solids (TDS) concentrations ranging from 28 to 100 mg L<sup>-1</sup>. In contrast, Cluster 2 includes samples S-RG4, S-RG5, and S-RG8, which show elevated TDS values (90 to 269 mg L<sup>-1</sup>). With the exception of S-RUP, S-RG4, and S-RG15, which record warmer temperatures from 1.43 to 3.19 °C, the remaining 16 samples in the June 2022 dataset exhibit colder temperatures, ranging from 0.03 °C to 0.67 °C (Fig. 6c). The most enriched samples are S-RG7, S-RG8, and S-RG10, with  $\delta^{18}$ O values between -23 % and -22.6 % vs. VSMOW in  $\delta^{18}$ O (Fig. 6d).

In June 2022, most of the springs were supplied by recent snowmelt, as indicated by low concentrations of mineral elements and cold temperatures. In contrast, S-RG8 and S-RG4 were supplied by groundwater, as evidenced by their higher concentrations of mineral elements.

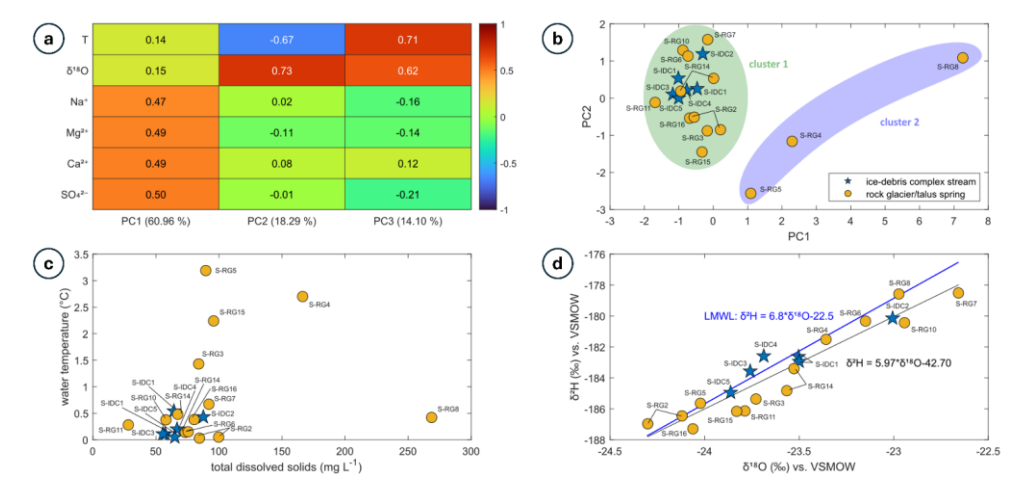


Fig. 6: (a) PCA scores for June 2022 samples. The explained variance for each PC is indicated in the legend of the horizontal axis. (b) Distribution of clusters formed from June 2022 samples following PCA and k-means clustering. Symbols represent different

sample types, and ellipses illustrate the distribution of each cluster. (c) Distribution of total dissolved solids (TDS) concentrations and water temperature for the June 2022 samples. (d) Isotopic composition of the June 2022 samples. Fig. 6: (a) PCA scores for June 2022 samples. Scores are displayed for PC1, PC2, and PC3, which together account for over 90% of explained variance. The six variables used in the analysis are water temperature (T), 8<sup>18</sup>O, Na<sup>+</sup>, Mg<sup>2+</sup>, Ca<sup>2+</sup>, and SO<sub>2</sub><sup>2+</sup> concentrations. The explained variance for each PC is indicated in the legend of the horizontal axis. (b) Distribution of clusters formed from June 2022 samples following PCA and k means clustering. Symbols represent different sample types, and ellipses illustrate the distribution of each cluster. (c) Distribution of total dissolved solids (TDS) concentrations and water temperature for the June 2022 samples. Symbols represent sample types. (d) Isotopic composition of the June 2022 samples. Symbols represent sample types. The black line represents the linear regression for the June 2022 samples, defined as  $\delta^2H = 5.97^*\delta^{18}O$  42.70. The blue line represents the nearest local meteoric water line (LMWL), established for the Whitehorse area, located 220 km east of the Shár Shaw Tagà catchment (Birks et al., 2004). This line is similar to the isotopic compositions found in the Lhù'aàn Mân' (Kluane Lake), 25 km east (Brahney et al., 2010).

#### Samples collected in August 2022

PC1 accounts for 60.57 % of the variance in the dataset and is strongly influenced by solute concentrations, with PC scores ranging from 0.47 to 0.48 (Fig. 7a). PC2, which explains 22.34 % of the variance, reflects opposing influences of temperature (0.68) and isotopic composition (-0.63). PC3, accounting for 9.01 % of the variance, shows joint positive correlations with both temperature (0.71) and isotopic composition (0.63).

Clustering analysis clearly distinguishes different sample types, forming 9 clusters, the maximum achievable based on the parametrization (Fig. 7b). Cluster 3 consists of glacial outlet samples, characterized by low solute concentrations (16 to 38 mg L<sup>-1</sup> in TDS), cold temperatures (0.06 to 0.07 °C), and depleted isotopic compositions (-21.6 to -22 % vs. VSMOW in  $\delta^{18}$ O) as seen in Figs. 7c and 7d. Clusters 5 and 6 comprise Shár Shaw Tagà River samples, with warmer temperatures (3.47 °C to 6.26 °C), higher solute concentrations (88 to 238 mg L-1 in TDS), and depleted isotopic compositions (-21.8 to -22.2 ‰ vs. VSMOW in  $\delta^{18}$ O). The distinction between these clusters may be attributed to variations in the glacial regime diurnal cycle and weather conditions based on sampling times. Clusters 4 and 8 include samples from springs near the upper end of the rock glacier front and at the transition area with the ice-debris complex (e.g., S-IDC5, S-RG1, S-RG2). As shown in Figs. 7c and 7d, these springs display high concentrations of mineral elements (209 to 304 mg L<sup>-1</sup> in TDS) and enriched isotopic compositions (-20.6 to -20.9 ‰ vs. VSMOW in δ18O). Clusters 2 and 9 are represented by springs S-RG7, S-RG8, S-RG9A, and S-IDC1, which exhibit high but narrow ranges of solute concentrations (282 to 309 mg L<sup>-1</sup> in TDS) and more depleted isotopic compositions (-21.6 to -21.8 ‰ vs. VSMOW in δ¹8O), as shown in Fig. 7d. Clusters 1 and 7 include other springs from the N1 subsection of the Shár Shaw Tagà River, which are characterized by low solute concentrations (111 to 162 mg L-1 in TDS) and enriched isotopic compositions (-20.4 to -20.9 \% vs. VSMOW in \delta^{18}O). Fig. 7d clearly distinguishes samples with depleted isotopic compositions (below -21.5 ‰ vs. VSMOW in δ<sup>18</sup>O) from those with enriched compositions (above -20.9 ‰ vs. VSMOW in  $\delta^{18}O$ ).

In late summer, the hydrochemical signatures of the springs show significant contrasts, with a high number of clusters. However, springs S-RG7, S-RG8, and S-RG9A share isotopic signatures similar to glacial meltwater from S-G1, S-G2, and

 S-G3, indicating a glacial input. Despite being located on opposite sides of the river, these springs cluster together, contrasting with the other springs. The high number of clusters among the other springs, with more enriched isotopic compositions, is likely due to different local drainage systems influenced by summer precipitation. Interactions between the groundwater sources of these two spring types may explain the varying clustering patterns and physicochemical values observed for RG-7 and RG-8. Most of the rock glacier spring samples show very cold temperatures (< 2 °C; Fig. 7c), suggesting proximity to massive ice or permafrost areas (e.g. Carturan et al., 2016).

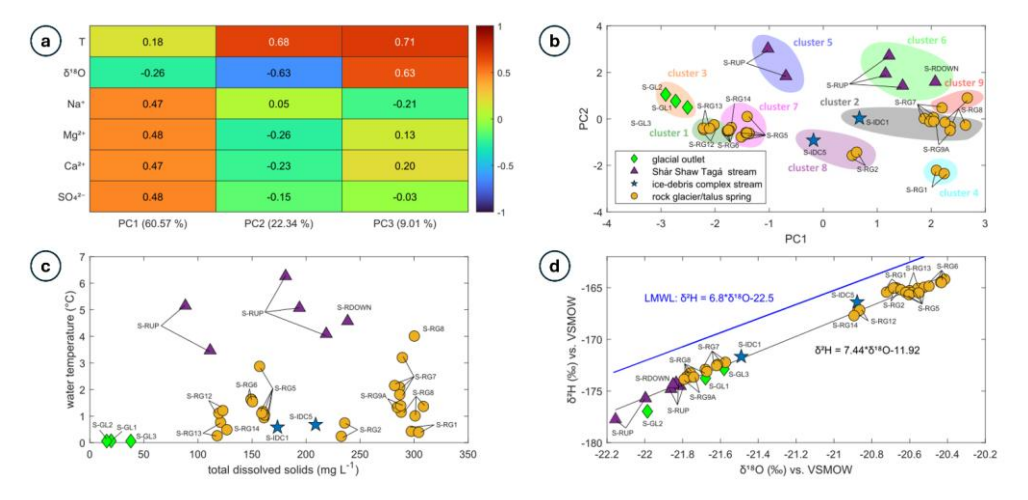


Fig. 7: (a) PCA scores for August 2022 samples. The explained variance for each PC is indicated in the legend of the horizontal axis. (b) Distribution of clusters formed from August 2022 samples following PCA and k-means clustering. Symbols represent different sample types, and ellipses illustrate the distribution of each cluster. (c) Distribution of total dissolved solids (TDS) concentrations and water temperature for the August 2022 samples. (d) Isotopic composition of the August 2022 samples. Fig. 7: (a) PCA scores for August 2022 samples. Scores are displayed for PC1, PC2, and PC3, which together account for over 90% of explained variance. The six variables used in the analysis are water temperature (T), \(\delta^{18}\)O, Na\(^1\), Mg\(^2\), Ca\(^2\), and SO\(^2\) concentrations. The explained variance for each PC is indicated in the legend of the horizontal axis. (b) Distribution of clusters formed from August 2022 samples following PCA and k-means clustering. Symbols represent different sample types, and ellipses illustrate the distribution of each cluster. (c) Distribution of total dissolved solids (TDS) concentrations and water temperature for the August 2022 samples. Symbols represent different sample types. (d) Isotopic composition of the August 2022 samples. Symbols represent sample types. The black line represents the linear regression for the August 2022 samples, defined as \(\delta^2\)H = 7.44\(\delta^{18}\)O 11.92. The blue line represents the nearest local meteoric water line (LMWL), established for the Whitchorse area, located 220 km east of the Sh\(\delta^2\) Sh was Tag\(\delta\) catchment (Birks et al., 2004). This line is similar to the isotopic compositions found in the Lh\(\delta^2\) And M\(\delta^2\) (Kluane Lake), 25 km east (Brahney et al., 2010).

Samples collected in June 2023

Formatted: Font: 9 pt, Bold

Formatted: Space After: 10 pt, Line spacing: single

487 PCA conducted on samples collected in June 2023 revealed that PC1 accounts for 68.79 % of the variance (Fig. 8a), primarily 488 driven by solute concentrations (PC scores ranging from 0.40 to 0.48). PC2 and PC3 explain 15.54 % and 10.43 % of the 489 variance, respectively. PC2 is mainly influenced by water temperature (0.88), while PC3 is dominated by isotopic composition 490 (0.86).491 The glacier outlet samples form a distinct cluster, labeled as Cluster 3 (Fig. 8b). The remaining samples are divided into two 492 clusters, with a clear distinction based on the maximum number of clusters (5). Cluster 1 consists solely of Shár Shaw Tagà 493 River samples from the upstream part of the N1 subsection. Cluster 2 includes spring samples and Shár Shaw Tagà River 494 samples collected in the downstream part of the N1 subsection. River samples from the downstream N1 subsection and spring 495 samples exhibit higher solute concentrations (from 121 to 147 mg L<sup>-1</sup> in TDS) and colder temperatures (from 0.7 to 4 °C, with 496 14 out of 16 samples < 2 °C) compared to the upstream N1 samples, which have lower solute concentrations (87 to 125 mg L 497 1) and warmer temperatures (5.3 to 9.5 °C; Fig. 8c). The isotopic composition is generally more enriched for the upstream N1 498 river samples than for the downstream N1 river and spring samples (Fig. 8d). The isotopic composition of one of the two 499 glacial water samples from G-B1 (sample S-GL1) is similar to the composition from the Shár Shaw Tagà River in upstream 500 N1 (water flowing from G-A1). However, the second S-GL1 sample shows a much more enriched isotopic composition, due 501 to a two-day interval between the respective samplings. The most enriched sample (-21.2 % vs. VSMOW in δ18O and -165.4 502 % vs. VSMOW in  $\delta^2$ H) was taken first, when the G-B1 glacier was still snow-covered. The most depleted sample (-22.4 %503 vs. VSMOW in  $\delta^{18}$ O and -173.6 % vs. VSMOW in  $\delta^{2}$ H) was taken two days later, following significant snowmelt cover on 504 G-B1 and the initiation of glacial melt. 505 The springs located on opposite sides of the river along the N1 subsection cluster together and exhibit similar close 506 hydrochemical signatures, similar to what was observed in August 2022. By distinguishing between two clusters, the PCA 507 highlights the important influence of these springs on the Shár Shaw Tagà River. Their outflows significantly lower the water 508 temperature and increase solute concentrations in the river.

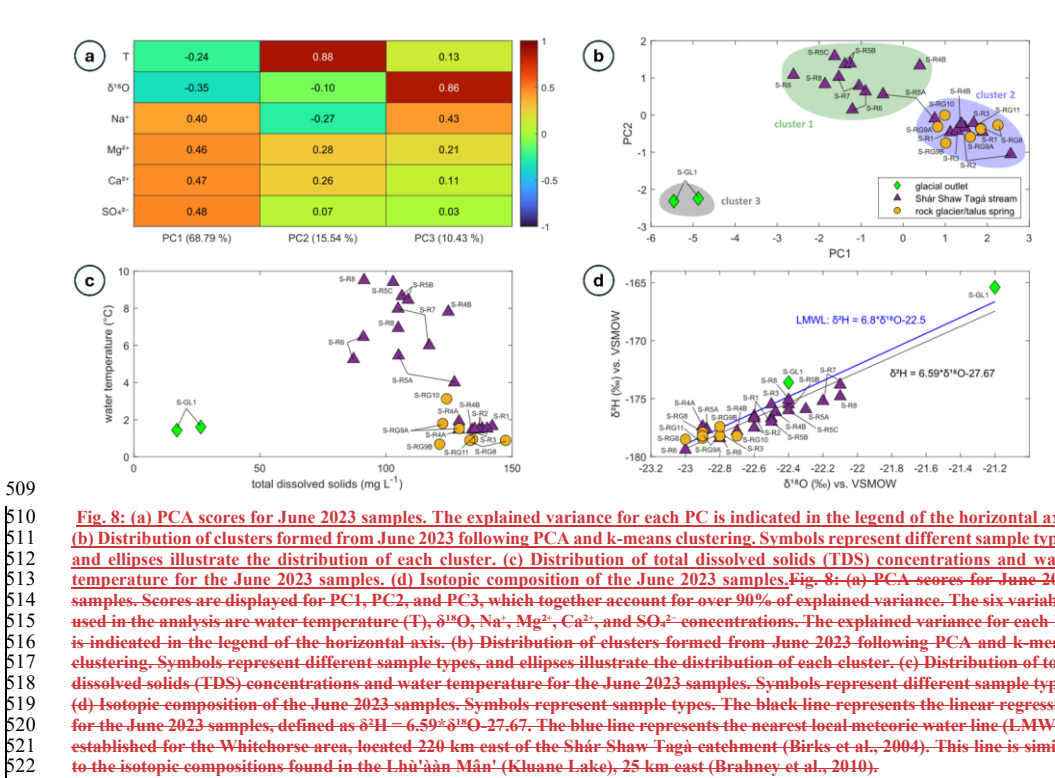


Fig. 8: (a) PCA scores for June 2023 samples. The explained variance for each PC is indicated in the legend of the horizontal axis. (b) Distribution of clusters formed from June 2023 following PCA and k-means clustering. Symbols represent different sample types, and ellipses illustrate the distribution of each cluster. (c) Distribution of total dissolved solids (TDS) concentrations and water temperature for the June 2023 samples. (d) Isotopic composition of the June 2023 samples. Fig. 8: (a) PCA scores for June 2023 samples. Scores are displayed for PC1, PC2, and PC3, which together account for over 90% of explained variance. The six variables used in the analysis are water temperature (T), \$0.80, Na\*, Mg2\*, Ca2\*, and SO4\* concentrations. The explained variance for each PC is indicated in the legend of the horizontal axis. (b) Distribution of clusters formed from June 2023 following PCA and k-means clustering. Symbols represent different sample types, and ellipses illustrate the distribution of each cluster. (c) Distribution of total dissolved solids (TDS) concentrations and water temperature for the June 2023 samples. Symbols represent different sample types. (d) Isotopic composition of the June 2023 samples. Symbols represent sample types. The black line represents the linear regression for the June 2023 samples, defined as δ<sup>2</sup>H = 6.59\*δ<sup>18</sup>O-27.67. The blue line represents the nearest local meteoric water line (LMWL), established for the Whitehorse area, located 220 km east of the Shar Shaw Tagà catchment (Birks et al., 2004). This line is similar to the isotopic compositions found in the Lhù'aan Man' (Kluane Lake), 25 km east (Brahney et al., 2010).

#### Synthesis of physico-hydrochemical characterisation

509

523 524

525

526

527

528

529

530

531

532

The springs surrounding RG-A1's front exhibit heterogeneous hydrochemical signatures. However, a group of springs along the N1 subsection (S-RG7, S-RG8, and S-RG9A) cluster together in PCA and share high EC values, depleted isotopic compositions, high solute concentrations, and similar radon activities. Despite being located on opposite sides of the river, these three springs show striking similarities, suggesting a common origin. Their isotopic compositions are comparable to those of glacial meltwater sampled at G-B1 and in the Shár Shaw Tagà River, differing significantly from other springs along RG-A1's front. The contribution of internal ice melt in rock glacier outflows is known to be minimal and does not significantly influence isotopic signatures (Croce and Milana, 2002; Krainer and Mostler, 2002; Krainer et al., 2007). This evidence supports the conclusion that S-RG7, S-RG8, and S-RG9A are springs fed by shallow groundwater of glacial origin. The other springs Formatted: Font: 10 pt

- around RG-A1's front exhibit diverse hydrochemical signatures under varying hydro-meteorological conditions. All springs
- consistently exhibit cold temperatures.
- During low-discharge periods, such as June 2023, the springs along the N1 subsection considerably increase downstream
- 536 solute concentrations and radon activities in the Shár Shaw Tagà River, while their cold outflows reduce stream temperature.
  - The other springs around RG-A1's front are primarily supplied by snowmelt in early summer and by summer precipitation in
- 338 late summer. Their diverse hydrochemical signatures and resulting clusters reflect varying local drainage systems within the
  - rock glacier. Springs at the front of RG-A1 consistently exhibit cold temperatures, indicating their proximity to ground ice.

#### 4.3 TIR survey

537

539

540

542

544

545

547

548

551

552

553

555

- 541 The TIR survey detected four cold water outflows outside the "narrow section" of the Shár Shaw Tagà River, located in the
  - outwash plain downstream of RG-A1 (Fig. 9). Two outflows were identified on the left bank: one associated with meltwater
- 543 originating from a snow patch at the front of RG-A1, and the other is from a persistent snow patch on the west flank of the
  - valley. The other two outflows were located on the right bank, originating from the middle of the outwash plain near the front
  - of RG-B2. These four outflows are not supplied by RG-A1, as they originate from snow patches or from the right bank.
- 546 The furthest downstream exfiltration area in the "narrow section" (TIR-L8) is situated in the N1 subsection, just a few meters
  - upstream of the bedrock outcrop (Fig. 9). Within the N1 subsection, eight groundwater exfiltration areas were identified on
  - the left bank of the main channel, and six on the right bank. Exfiltration areas on the left bank are generally smaller, with
- 549 plume lengths ranging from 1 to 6 m, four of these less than 2 m long. In contrast, exfiltration areas on the right bank are larger,
- 550 with plume lengths ranging from 5 to 14 m, and four exceed 10 m in length. These exfiltration areas were clearly visible as
  - color contrasts, distinguishing the warmer surface waters from the colder groundwater exfiltrations (Fig. 10a). The positions
  - of the mixing plumes were observed at each location. In the most notable exfiltration areas (plume lengths > 2 m), clearer
  - water was observed in the visible video footage, facilitating the validation of groundwater exfiltration detection (Fig. 10b).
- 554 Two of the six groundwater exfiltration areas detected from the right bank can be associated with springs sampled and
  - measured during the 2022 and 2023 campaigns for physico-hydrochemical analysis (TIR-R2 and TIR-R3 correspond to S-
- 556 RG9A and S-RG9B, respectively). As mentioned in Sect. 2, depending on the river level and meteorological conditions, the
- 557 outflow locations of the springs on the left side of the river have been observed to shift 10 to 20 m downstream of the RG-A1
- front. During the TIR survey, these conditions were met, and no exfiltration area was found directly at the location of a spring
  - sampled in 2022 and 2023. Instead, exfiltration areas on the left bank were detected 20 m downstream of their corresponding
- 560 springs sampled earlier. Therefore, exfiltration areas TIR-L1, TIR-L2 and TIR-L8 can be associated with the springs S-RG8,
- S-RG10 and S-RG11, respectively (Fig. 9).
- 562 The drone-based TIR survey identified a high density of cold groundwater exfiltrations from both the left and right banks of
- 563 the N1 subsection of the Shár Shaw Tagà River, upstream of the bedrock outcrop. Exfiltration areas on the right bank exhibited



Fig. 9: Location of cold water outflows detected by the TIR survey along the Shár Shaw Tagà riverbed. The zoomed-in view of the "narrow section" highlights an area with a high density of cold groundwater outflows detected on both sides of the river, upstream of a bedrock outcrop constraining the riverbed. Additional cold water outflows are observed in the downstream outwash plain, originated from either snow patch melt on the left side or from the right bank of the outwash plain. Springs that outflow from RG-A1 or the opposite talus slope and were sampled during the 2022 and 2023 campaigns are marked in the zoomed-in panel. Basemap credits: Esri.Fig. 9: Location of cold water outflows detected by the TIR survey along the Shár Shaw Tagà riverbed. The zoomed-in view of the "narrow section" highlights an area with a high density of cold groundwater outflows detected on both sides of the river, upstream of a bedrock outcrop constraining the riverbed. Additional cold water outflows are observed in the downstream outwash plain, originated from either snow patch melt on the left side or from the right bank of the outwash plain. Springs that outflow from RG-A1 or the opposite talus slope and were sampled during the 2022 and 2023 campaigns are marked in the zoomed-in panel. The spring locations represent the positions of their outflows during the August 2022 campaign, though these may shift depending on hydro-meteorological conditions and river level. The bedrock outcrop marks the division of the "narrow section" of the Shár Shaw Tagà River into two subsections, N1 and N2, as shown on the map. Basemap credits: Esri.

Formatted: Space After: 10 pt, Line spacing: single

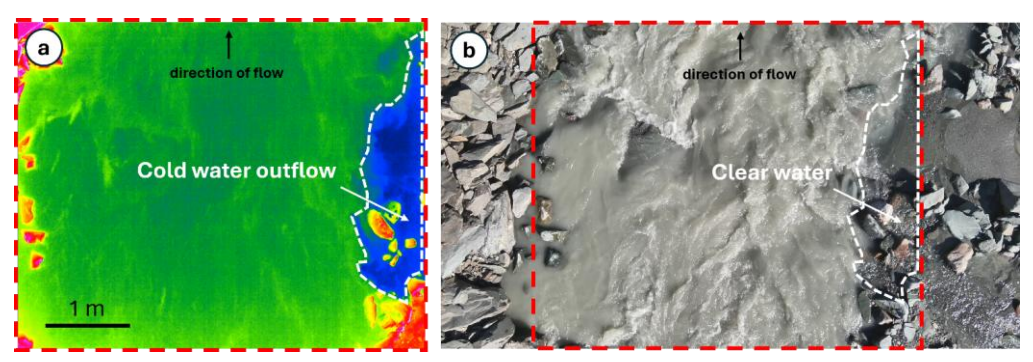


Fig. 10: (a) TIR capture showing cold groundwater outflow (in blue, delimited by the dashed white line), mixing with the warmer waters of the Shár Shaw Tagà River (in green) at the TIR-R2 location. Note that the video does not provide a color scale. (b) RGB image capture showing clear water outflowing into the Shár Shaw Tagà River, which is characterized by a significant sediment load at the TIR-R2 location. The cold water area detected with TIR is delimited by the dashed white line. The extent of the TIR capture is indicated by the dashed red line. Flight data and information can be accessed as Supplemental Material in Charonnat and Baraer, 2025

### 5 DISCUSSION

#### 5.1 The rock glacier forces resurgence of shallow groundwater flow

The preliminary inventory of springs and the TIR survey identified a high density of spring outflows from both banks of the N1 subsection of the Shár Shaw Tagà River. The physico-hydrochemical characterization indicates that the springs on both banks share a similar signature; originating from glacial melt, suggesting a common source (Fig. 7 and 8). The contribution of internal ice melt in rock glacier outflows is known to be minimal and does not significantly influence isotopic signatures (Croce and Milana, 2002; Krainer and Mostler, 2002; Krainer et al., 2007). This evidence supports the conclusion that these springs are fed by groundwater of glacial origin. In June 2023, a low-discharge period, field observations revealed river water losses before entering the upstream outwash plain, where the riverbed temporarily lacked surface flow. Surface flow resumed only from the N1 subsection due to groundwater inflows, pointing to the existence of shallow subsurface flow through the upstream outwash plain. Together, these elements indicate that water outflowing from the springs along the N1 subsection resurges from lateral shallow groundwater, likely infiltrating through the riverbed and flowing within the lateral alluvial aquifer before resurfacing.

Contrary to initial hypotheses, no evidence was found of outflow originating from the head of the rock glacier's subcatchment (comprising glaciers G-B1 and G-B2). Instead, the physico-hydrochemical characterization suggests that glacial meltwater entering the water to the river derives from upstream outwash plains of the main Shár Shaw Tagà catchment. In contrast, the other springs emerging at the front of the rock glacier appear to be linked to internal drainage systems within the rock glacier

itself. These springs are primarily fed by snowmelt in the early season and by summer precipitation later in the season, with

minimal or negligible glacier melt contribution, as shown by the physico-hydrochemical characterization of the samples collected in June 2022 and August 2022, respectively. Across Canada, precipitation is typically enriched in heavy isotopes during the snow-free period and depleted during winter and spring (Gibson et al., 2020). Accordingly, the depleted isotopic compositions, low solute concentrations, and cold temperatures measured in early June point to a snowmelt origin, while the enriched isotopic compositions in August reflect a stronger influence from rainfall. This seasonal distinction is further supported by contrasting results from springs in the N1 subsection, which exhibit characteristics of both groundwater and glacier-fed sources. Some springs likely reflect a mix of these sources, with their physicochemical parameters and clustering reflecting these dual influences depending on hydro-meteorological conditions and time periods. Contrary to initial hypotheses, no evidence was found of outflow supplied by the head of the rock glacier's subcatchment (comprising glaciers G-B1 and G-B2). The physico-hydrochemical characterization instead suggests that glacial meltwater outflowing to the river originates from the upstream outwash plains of the main Shár Shaw Tagà catchment. The characterization of the other springs at the rock glacier's front suggests that they are linked to local drainage systems within the rock glacier. They are supplied by snowmelt in early season and summer precipitation in late season, with minimal or negligible glacier melt contribution, as shown by the physico-hydrochemical characterization of the samples from June 2022 and August 2022, respectively. Some springs may be influenced by both systems, with their physicochemical parameters and clustering reflecting these dual influences depending on hydro-meteorological conditions and time periods.

Parafluvial flow is common in outwash plains with coarse-grained unconsolidated sediments, occurring in river reaches where water is lost before rejoining the river in gaining reaches (Cartwright and Hofmann, 2016). Outwash plains, often underlain by bedrock, retaining groundwater in the shallow subsurface, providing baseflow during dry periods when upstream discharge is limited (Müller et al., 2024). Fractured and faulted bedrock aquifers can further contribute to baseflow in outwash plains (Hayashi, 2019; Müller et al., 2022). In this case, the resurgence of parafluvial and shallow groundwater flow is visible during dry periods. The dynamic location of the springs reported between sampling campaigns reflects the lateral and vertical extent of the alluvial aquifer. The lower density of springs identified beyond the bedrock outcrop at the end of the N1 subsection suggests a shallow bedrock interface with limited groundwater flow capacity. Additionally, the faults inferred along the riverbed in previous geological studies (Dodds and Campbell, 1992) may facilitate groundwater flow from outwash plains upstream of the rock glacier to the N1 subsection, where it is forced to resurge.

The cold temperatures measured in the springs of the N1 subsection indicate that outflows from the alluvial aquifer are cooled by adjacent frozen content, such as massive ice or permafrost (e.g. Carturan et al., 2016). The cold temperatures measured in the springs of the N1 subsection indicate that outflows from the alluvial aquifer are cooled by adjacent frozen content. Frozen content has been confirmed in the rock glacier by Evin et al. (1997), and is suspected for the talus slope, based on Scapozza, (2015). The frozen content on both sides of the Shár Shaw Tagà River constrains the alluvial aquifer, forcing groundwater to resurface through springs and cold water upwellings in the riverbed. The advance of the rock glacier, which considerably

narrows the riverbed, further enforces this constraint. The younger lobes of the rock glacier, potentially containing higher amounts of frozen content, extend north from the bedrock outcrop to the downstream outwash plain, possibly acting as an additional barrier to groundwater flow where they border the Shár Shaw Tagà River. Thus, the location of the resurgences in the N1 subsection can be explained by the geomorphic properties of the rock glacier. The narrowing of the riverbed by the rock glacier's advance and the presence of frozen content constrain the riverbed, forcing the resurgence of shallow groundwater flow.

#### 5.2 The rock glacier affects downstream cryo-hydrological processes and hydrological continuity

The proximity of bedrock and ground ice in the narrow section of the Shár Shaw Tagà River critically reduces the width and depth of the alluvial aquifer, leading to groundwater exfiltrations along the N1 subsection, as discussed in Sect. 5.1. Aufeis typically develop in areas where river flow velocity decreases, such as braided channels and outwash plains (Hu and Pollard, 1997). The TL monitoring suggests that the resurgences from the alluvial aquifer provide the water from the N1 subsection but the decrease in river flow velocity and channel depth creates conditions favourable for the formation of aufeis in the outwash plain immediately downstream of the rock glacier. In contrast, the steeper slope in the N1 subsection likely inhibits aufeis formation directly at the springs locations. The TL monitoring suggests that the resurgences from the alluvial aquifer, in combination with a decrease in river flow velocity and channel depth in the outwash plain immediately downstream of the rock glacier, contribute to the formation of aufeis. Thus, the rock glacier plays a significant role in influencing downstream cryo-hydrological processes.

The high density of springs along the N1 subsection and their distinct physicochemical signatures substantially affect the downstream Shár Shaw Tagà River. The solute enrichment observed in these springs is attributed to water-rock interactions along groundwater flow paths. Prolonged residence time in aquifers facilitates the accumulation of dissolved solutes (Hem, 1985). In addition, the springs may be partially connected to internal drainage systems within the rock glacier, which are known to generate solute-rich outflows (Colombo et al., 2018). Lastly, the proximity to buried ground ice and permafrost—both within the rock glacier and in adjacent talus slopes—may enhance the release of mineral elements through thermal erosion of the ice-sediment matrix (Jones et al., 2019). The physico-hydrochemical characterization from June 2023 demonstrates that during dry periods, these springs notably increase solute concentrations and radon activities, while simultaneously cooling the river water. These findings are consistent with prior studies showing the influence of rock glaciers on the physicochemical characteristics of downstream surface waters (e.g., Bearzot et al., 2023; Brighenti et al., 2023; Robinson et al., 2022; Wagner et al., 2021). However, the rock glacier in this study alters the entire riverbed and its physicochemical parameters primarily due to its geomorphic properties. Contrary to initial hypotheses based on early observations and the literature, its internal hydrological behavior does not account for the critical impact the rock glacier has on the riverbed's hydrological system.

# 5.3 Future evolution of the rock glacier influence on catchment hydrology

Predicting the future evolution of the system described in Sect. 5.1 and 5.2 is challenging. However, several scenarios across different timescales can be envisioned. Frozen content is likely to persist in depositional landforms for extended periods, as residual ice has been detected in rock glaciers below the modeled elevation limit in multiple cases (e.g., Carturan et al., 2024; Colucci et al., 2019). Future hydrological conditions in alpine catchments will likely be characterized by a reduced hydrological influence of glaciers, lower discharge and an increased contribution from groundwater and periglacial features to streamflow (Huss et al., 2017; Jones et al., 2019; Zierl and Bugmann, 2005). These conditions were observed during the June 2023 sampling campaign, which occurred after the peak of snowmelt and prior to the peak of glacial ablation, leading to a substantial influence of groundwater resurgences on the Shár Shaw Tagà River. Similar conditions may be expected in the future, with groundwater outflows caused by the rock glacier expected to gain influence in the Shár Shaw Tagà River. However, the degradation of frozen content around the riverbed may alter this scenario, as rising air temperatures continue to drive permafrost thaw. Additionally, thermal and mechanical erosion caused by lateral groundwater flow could expand the parafluvial zone and create alternative subsurface flow paths, reducing the hydrological discontinuity and disruptive effects of the rock glacier.

The absence of evident streamflow contribution from the G-B1 subcatchment to the Shár Shaw Tagà River, as highlighted in Sect. 5.1, suggests substantial deep infiltration of surface and shallow groundwater flow between the glaciers of the subcatchment and the rock glacier. Although the role of rock glaciers in deep infiltration has not been thoroughly documented to our knowledge, it is suggested that their high vertical and horizontal flow transmissivity may enhance infiltration into deep aquifers and groundwater recharge (Navarro et al., 2023). From a broader perspective, it is considered that deep groundwater systems link mountain cryosphere components to lowlands aquifers through mountain-block recharge (van Tiel et al., 2024). In this context, increased infiltration due to glacial retreat and permafrost degradation may position rock glaciers and other depositional features as critical hubs in proglacial areas, contributing to regional groundwater circulation and water resources.

#### 5.4 Limitations and perspectives

The physico-hydrochemical characterization conducted in this study was based on three sampling campaigns under varying hydro-meteorological conditions. These diverse settings posed several challenges for water sampling, including issues with accessibility, safety concerns, periods of no flow, and the need to prioritize specific areas. As a result, some sampling sites could not be revisited during every campaign, leading to gaps in the data over time. Moreover, fluctuating weather conditions during a single campaign in proglacial environments likely contributed to variations in physicochemical parameters at some sites. Where possible, multiple samples were taken at different times or on different days within the same campaign to minimize biases caused by diurnal and meteorological variations. Consequently, some sites could not be compared across campaigns, and their characterization can remain incomplete. On the other hand, these challenges allowed us to identify the varying influences of different drainage systems on certain springs.

Upon initial observations and hypotheses, we adopted a unique multi-method approach, which evolved as we refined our understanding of the system. While this combination of methods was crucial in addressing the research question and drawing the conclusions presented, alternative approaches could have provided a more direct route to the findings. Future research could build on the insights gained in this study by investigating the hydrological roles of other rock glaciers within the same valley or in different regions. Such studies would help assess whether similar patterns occur across varying settings. Moreover, this research underscores the potential role of the rock glacier and adjacent depositional features in facilitating the infiltration of water into deep groundwater systems, as suggested by the lack of water outflow from the head of the subcatchment to the the Shár Shaw Tagà River. Characterizing these transfers is crucial for understanding the role of proglacial areas in water resource supply during deglaciation. The authors strongly encourage further works in this direction.

#### 6 CONCLUSIONS

The geomorphic properties of rock glaciers make them dynamic features capable of altering riverbed hydrological systems. As assessed in this study, rock glaciers can obstruct proglacial outwash plains, thereby controlling and constraining shallow groundwater flow. This obstruction results in channel confinement, which induces resurgences from the alluvial aquifer, with profound impacts on both the hydrochemistry and hydrogeomorphology of alpine catchments. Rock glacier disruption leads to substantial changes in the physicochemical parameters of streamflow, and contributes to the formation of aufeis, a consequence not previously documented in the literature.

In contrast to initial hypotheses, the internal hydrological system of the rock glacier does not exhibit a significant influence on downstream surface waters. Instead, the critical disruption to the riverbed hydrological system is due to the geomorphic constraint imposed by the rock glacier on the alluvial aquifer. The water that flows from the subcatchment above the rock glacier is suspected to infiltrate deep groundwater systems through the rock glacier and the adjacent depositional features, as it could not be traced beyond the rock glacier.

Thus, this study emphasizes the complexity and potentially misleading nature of characterizing groundwater flow pathways in proglacial environments. The findings also have broader implications for mountain hydrology and water resources, highlighting the importance of rock glaciers and proglacial systems as critical hydrological features and potential hubs for mountain-block recharge, linking the mountain cryosphere to deep groundwater systems.

# Appendix: Table A1

<b>A</b>					Dates and times of	of sampling	
Sampling	Northing	Easting	Elevation	Comments	June 2022	August 2022	June 2023
sites	<u>(UTM)</u>	(UTM)	(m a.s.l.)				

Formatted: Font: 8 pt
Formatted: Font: 8 pt

S-R1	6773938	601332	1738	Shár Shaw Tagà river (narrow	NV	NV	15/06/23 12:50	1
				section)			<u>16/06/23 13:00</u>	
S-R2	6773933	601336	1739	Shár Shaw Tagà river (narrow	NV	NV	15/06/23 13:07	1
				section)			<u>16/06/23 13:10</u>	
S-R3	6773933	601336	1739	Shár Shaw Tagà river (narrow	NV	NV	15/06/23 13:25	1
				section)			16/06/23 13:40	
S-R4A	6773813	601409	1741	Shár Shaw Tagà river (narrow	NV	NV	15/0 <u>6/23 13:50</u>	-
				section)				
S-R4B	6773817	601408	1746	Shár Shaw Tagà river (narrow	NV	NV	15/06/23 14:35	-
				section)			16/06/23 14:20	
S-R5A	6773817	601408	1746	Shár Shaw Tagà river (narrow	NV	NV	15/06/23 14:40	1
				section)			<u>16/06/23 15:10</u>	
S-R5B	6773817	601408	1746	Shár Shaw Tagà river (narrow	NV	NV	15/06/23 14:10	4
				section)			16/06/23 15:25	
S-R5C	6773781	601407	1747	Shár Shaw Tagà river (narrow	NV	NV	16/06/23 14:45	-
<u>B RSC</u>	0775701	001107	17-17	section)	111	111	10/00/25 14:45	
S-R6	6773685	601449	1759	Shár Shaw Tagà river (narrow	NV	NV	15/06/23 16:40	-
3-10	0773063	001442	1737	section)	IVV	IVV	16/06/23 15:45	
S-R7	6773691	601445	1753	Shár Shaw Tagà river (narrow	NV	NV	15/06/23 16:50	T
3-K/	07/3091	001443	1/33	section)	INV	INV	16/06/23 16:00	
C DO	(7772 (01	601445	17752		207	NII.		$\top$
<u>S-R8</u>	6773691	601445	1753	Shár Shaw Tagà river (narrow	NV	NV	15/06/23 17:00	_
				section)			16/0 <mark>6/23 16:10</mark>	+
S-RDOWN	6774302	600936	1687	Shár Shaw Tagà river (downstream	<u>NV</u>	19/08/22 13:05	NV	+
				<u>floodplain</u> )				
S-RUP	6773641	601455	1749	Shár Shaw Tagà river (upstream	NV	16/08/22 12:00	NV	_
				<u>floodplain</u> )		16/08/22 16:16		+-
						17/08/22 13:12		+
						18/08/22 12:35		+'
0.011	(7722200	600000	2002	, C.P.I	207	19/08/22 13:01	10/06/22 14 25	+'
S-GL1	6772289	600889	2083	stream at G-B1 snout	NV	18/08/22 18:36	19/06/23 14:35	_
							21/06/23 12:05	$\vdash$
S-GL2	6772230	600819	2109	stream at G-B1 snout	NV	18/08/22 18:06	NV	_
S-GL3	6772239	600703	2086	stream at G-B1 snout	NV	18/08/22 19:03	NV	_
S-IDC1	6772896	600330	1886	ice-debris complex stream	16/06/22 15:56	18/08/22 20:29	NV	-
					18/0 <u>6/22 17:50</u>			+

	Formatted: Font: 8 pt
	Formatted
	Formatted: Font: 8 pt
	Formatted
	Formatted: Font: 8 pt
	Formatted
	Formatted: Font: 8 pt
	Formatted
	Formatted: Font: 8 pt
	Formatted
	Formatted: Font: 8 pt
	Formatted
	Formatted: Font: 8 pt
	Formatted
	Formatted: Font: 8 pt
	Formatted
	Formatted: Font: 8 pt
	Formatted
	Formatted: Font: 8 pt
	Formatted
	Formatted: Font: 8 pt
	Formatted
	Formatted: Font: 8 pt
	Formatted
	Formatted: Font: 8 pt
1	Formatted
1	Formatted: Font: 8 pt
	Formatted
	Formatted
	Formatted: Font: 8 pt
	Formatted
	Formatted: Font: 8 pt
	Formatted
	Formatted: Font: 8 pt
	Formatted
١	Formatted

S-IDC2	6772897	600330	1886	ice-debris complex stream	18/06/22 17:56	NV	NV	7
S-IDC3	6772943	600345	1891	ice-debris complex stream	16/06/22 15:37	NV	NV	-
				•				
S-IDC4	6772967	600379	1893	ice-debris complex stream	<u>16/06/22 17:04</u>	NV	NV	-
<u> </u>	0112301	000377	10,5	ioo deerib compier stream	10/0/3/22 17/01		111	$\top$
S-IDC5	6773216	600703	1860	ice-debris complex stream	16/06/22 17:40	18/08/22 20:55	NV	-
<u>p-ibcs</u>	0773210	000703	1800	ice-debits complex stream	10/00/22 17:40	16/05/22 20:33	IVV	_
C DC1	6773340	601180	1797	spring at RG-A1 front	NV	17/08/22 11:58	NV	_
S-RG1	0773340	001180	1/9/	spring at KG-A1 front	INV	18/08/22 13:52	INV	_
						_		_
S-RG2	6773415	601279	1780	spring at RG-A1 front	12/06/22 16:54	16/08/22 11:15	NF	
					<u>19/06/22 15:08</u>	17/08/22 12:14		_
S-RG3	6773442	601378	1770	spring at RG-A1 front	19/06/22 14:48	NF	NF	$\perp$
								`
S-RG4	6773492	601414	1770	spring at RG-A1 front	19/06/22 13:52	NF	NF	_
S-RG5	6773643	601423	1770	spring at RG-A1 front	19/06/22 13:45	16/08/22 11:30	NV	-
						16/08/22 16:04		
						17/08/22 12:44		
						18/08/22 12:47		
						19/08/22 13:46		
S-RG6	6773683	601421	1758	spring at RG-A1 front	19/06/22 13:30	16/08/22 12:40	NV	
						17/08/22 13:05		
						<u>18/08/22 12:27</u>		
						19/08/22 13:24		
S-RG7	6773736	601413	1746	spring at RG-A1 front	19/06/22 13:18	16/08/22 13:05	NV	
						<u>17/08/22 13:58</u>		
						18/ <b>0</b> 8/22 12:14		
						<u>19/08/22 13:12</u>		_/
S-RG8	6773763	601408	1744	spring at RG-A1 front	19/06/22 12:50	16/08/22 13:15	15/06/23 14:55	_
						17/08/22 14:13	16/06/23 14:35	
						<u>18/08/22 11:11</u>		_/
						<u>19/08/22 12:34</u>		_/
S-RG9A	6773762	601415	1752	spring flowing from talus opposite	NV	16/08/22 12:13	15/06/23 14:55	
				to RG-A1 front (right bank)		17/08/22 13:29	16/06/23 14:25	+
S-RG9B	6773931	601335	1734	spring from talus opposite to RG-	NV	NV	16/06/23 14:10	1
				A1 front (right bank)				
S-RG10	6773778	601401	1749	spring at RG-A1 front	19/06/22 12:43	NV	16/06/23 14:00	l
		1	1					

+	Formatted
+	Formatted
	Formatted
+	Formatted
	Formatted
1	Formatted
-	Formatted
	Formatted
-	Formatted
1	Formatted
1	Formatted
Y	Formatted
1	Formatted
	Formatted
*	Formatted
+	Formatted
	Formatted
>	Formatted
1	Formatted
+	Formatted
1	Formatted
1	Formatted
	Formatted
1	Formatted
	Formatted
	Formatted
1	Formatted
+	Formatted
1	Formatted
	Formatted
+	Formatted
	Formatted
\	Earmattad

S-RG11	6773867	601367	1738	spring at RG-A1 front	19/06/22 12:35	NV	16/06/23 13:30
<u>D ROII</u>	0773007	001307	1750	Spring at ICO 711 Hone	15/ 00/22 12:55	144	10/05/25 15.50
S-RG12	6773971	601281	1726	spring at RG-A1 front	NV	18/08/22 11:56	NV
						19/08/22 12:10	
S-RG13	6773995	601265	<u>1726</u>	spring at RG-A1 front	<u>NV</u>	16/08/22 13:47	NV
						18/08/22 11:40	
S-RG14	6774166	601183	1712	spring at RG-A1 front	15/06/22 15:30	19/08/22 12:30	NV
					19/06/22 14:25		
S-RG15	6774210	600985	1683	spring at RG-A1 front	19/06/22 15:17	NV	NV
S-RG16	6774034	600854	1740	spring at RG-A1 front	19/06/22 15:42	NV	NV

Table A1: List and description of sites sampled during the three campaigns between June 2022 and August 2023, with UTM coordinates, elevation, dates and times of sampling. Samples are categorized into four distinct types: glacial outlets from the G-B1 glacier snout (S-GL#), ice-debris complex streams in the proglacial area between the glacier tongue and rock glaciers (S-IDC#), Shár Shaw Tagà River (S-R#), and springs from RG-A1 rock glacier front and opposite talus (S-RG#). Sites were not all sampled for every campaign, due to diverse reasons (access and safety issues, no flow, campaign dedicated to a specific area, etc.). When possible, sites were sampled several times to trace potential fluctuations in their physico-chemical signature. When not sampled, the comment "NV" stands for "not visited." The comment "NF," for "no flow," indicates a site not sampled as it was dry when visited.

### Code/Data availability

The data supporting this study are available upon request to the corresponding author.

# Video supplement

The videos and flight data used for the TIR analysis are available as Supplemental Material in Charonnat and Baraer, 2025, on Borealis dataverse (https://doi.org/10.5683/SP3/O57OMY).

#### Author contribution

Conceptualization: B.C. and M.B. Data curation: B.C. Formal analysis: B.C., M.B., J.M.-D. and C.M. Funding acquisition: M.B. and J.M.M. Investigation: B.C., M.B., E.V., J.M.-D., K.W. and E.D. Methodology: B.C., M.B., E.V. and J.M.-D. Project administration: B.C., M.B., E.V. and J.M.-D. Supervision: M.B., J.M.-D. and J.M.M. Visualization: B.C. and K.W. Writing – original draft preparation: B.C. Writing – review & editing: B.C., M.B., E.V., J.M.-D., C.M., K.W., E.D. and J.M.M. All authors have read and agreed to the published version of the manuscript.

# Competing interests

The authors declare that they have no conflict of interest.

Formatted: Font: 8 pt
Formatted: Font: 8 pt

# 754 Acknowledgements

756

758

759

762

- 755 We are grateful to the Kluane First Nation and the White River First Nation for the opportunity to conduct research on their
  - territory. We thank the Arctic Institute of North America and the University of Calgary for providing us service and access to
- 757 their facilities at Kluane Lake Research Station. We thank Parks Canada for their collaboration and for issuing permits that
  - allowed us to conduct research within Kluane National Park and Reserve.

#### 760 Financial support

- 761 This research was supported by the Natural Sciences and Engineering Research Council of Canada, grant numbers RGPIN-
  - 2020-05612 and RGPNS-2020-05612, and by Natural Resources Canada—Polar Continental Shelf Program, grant number
- 763 62723. Additional funding for the expedition was provided by the Research Centre on the Dynamics of the Earth System
- 764 (GEOTOP).

# 765 References

- 766 Abolt, C., Caldwell, T., Wolaver, B., and Pai, H.: Unmanned aerial vehicle-based monitoring of groundwater inputs to surface
- waters using an economical thermal infrared camera, Optical Engineering, 57(05), 1, https://doi.org/10.1117/1.oe.57.5.053113,
- 768 2018.
- 769 Antonelli, M., Klaus, J., Smettem, K., Teuling, A. J., and Pfister, L.: Exploring Streamwater Mixing Dynamics via Handheld
- Thermal Infrared Imagery, Water, 9(5), Article 5, https://doi.org/10.3390/w9050358, 2017.
- 771 Arenson, L. U., Harrington, J. S., Koenig, C. E. M., and Wainstein, P. A.: Mountain Permafrost Hydrology—A Practical
- Review Following Studies from the Andes, Geosciences, 12(2), Article 2, https://doi.org/10.3390/geosciences12020048, 2022.
- 773 Arenson, L., Hoelzle, M., and Springman, S.: Borehole Deformation Measurements and Internal Structure of Some Rock
- Glaciers in Switzerland, Permafrost and Periglacial Processes, 13, 117–135, https://doi.org/10.1002/ppp.414, 2002.
- Programmer Baker, E. A., Lautz, L. K., Kelleher, C. A., and McKenzie, J. M.: The importance of incorporating diurnally fluctuating stream
- 1 776 discharge in stream temperature energy balance models, Hydrological Processes, 32(18), 2901–2914,
- wiseling in steam temperature energy summer models, Tryansington Treesses, 32(10
- 777 <u>https://doi.org/10.1002/hyp.13226</u>, 2018.
- Baraer, M., McKenzie, J., Bury, J., and Knox, S.: Characterizing contributions of glacier melt and groundwater during the dry
- 779 season in a poorly gauged catchment of the Cordillera Blanca (Peru), Advances in Geosciences, 22, 41-49,
- 780 https://doi.org/10.5194/adgeo-22-41-2009, 2009.
- Baraer, M., McKenzie, J., Mark, B. G., Gordon, R., Bury, J., Condom, T., Gomez, J., Knox, S., and Fortner, S. K.: Contribution
- 782 of groundwater to the outflow from ungauged glacierized catchments: A multi-site study in the tropical Cordillera Blanca,
- 783 Peru, Hydrological Processes, 29(11), Article 11, <a href="https://doi.org/10.1002/hyp.10386">https://doi.org/10.1002/hyp.10386</a>, 2015.

Formatted: Indent: Left: 0 cm

Formatted: Font: Not Italic

Formatted: Font: Not Italic

Field Code Changed

- Barclay, J. R., Briggs, M. A., Moore, E. M., Starn, J. J., Hanson, A. E. H., and Helton, A. M.: Where groundwater seeps:
- 785 Evaluating modeled groundwater discharge patterns with thermal infrared surveys at the river-network scale, Advances in
- 786 Water Resources, 160, 104108, <a href="https://doi.org/10.1016/j.advwatres.2021.104108">https://doi.org/10.1016/j.advwatres.2021.104108</a>, 2022.
- 787 Barsch, D.: Rockglaciers: Indicators for the present and former geoecology in high mountain environments, 1996.
- 788 Bearzot, F., Colombo, N., Cremonese, E., di Cella, U. M., Drigo, E., Caschetto, M., Basiricò, S., Crosta, G. B., Frattini, P.,
- Freppaz, M., Pogliotti, P., Salerno, F., Brunier, A., and Rossini, M.: Hydrological, thermal and chemical influence of an intact
- 790 rock glacier discharge on mountain stream water, Science of The Total Environment, 876, 162777,
- 791 <u>https://doi.org/10.1016/j.scitotenv.2023.162777</u>, 2023.
- 792 Birks, S. J., Edwards, T. W. D., Gibson, J. J., Drimmie, R. J. and Michel, F. A.: Canadian network for isotopes in Precipitation,
- 793 http://www.science.uwaterloo.ca/~twdedwar/cnip/cniphome.html, 2004.
- 794 Blöthe, J. H., Rosenwinkel, S., Höser, T., and Korup, O.: Rock-glacier dams in High Asia, Earth Surface Processes and
- 795 Landforms, 44(3), 808–824, https://doi.org/10.1002/esp.4532, 2019.
- 796 Bodin, X., Schoeneich, P., Deline, P., Ravanel, L., Magnin, F., Krysiecki, J.-M., and Echelard, T.: Le permafrost de montagne
- 797 et les processus géomorphologiques associés: Évolutions récentes dans les Alpes françaises, Journal of Alpine Research |
- 798 Revue de géographie alpine, 103–2, <a href="https://doi.org/10.4000/rga.2806">https://doi.org/10.4000/rga.2806</a>, 2015.
- 999 Bolch, T., and Marchenko, S.: Significance of glaciers, rockglaciers and ice-rich permafrost in the Northern Tien Shan as water
- towers under climate change conditions, IHP/HWRP-Berichte, 8, Article 8, https://doi.org/10.5167/uzh-137250, 2009.
- 801 Brahney, J., Clague, J. J., Edwards, T. W. D., and Menounos, B.: Late Holocene paleohydrology of Kluane Lake, Yukon
- 802 Territory, Canada, Journal of Paleolimnology, 44(3), 873-885, https://doi.org/10.1007/s10933-010-9459-8, 2010.
- 803 Briggs, M. A., Hare, D. K., Boutt, D. F., Davenport, G., and Lane, J. W.: Thermal infrared video details multiscale groundwater
  - discharge to surface water through macropores and peat pipes, Hydrological Processes, 30(14), 2510-2511,
- 805 <u>https://doi.org/10.1002/hyp.10722</u>, 2016.

- B06 Brighenti, S., Engel, M., Dinale, R., Tirler, W., Voto, G., and Comiti, F.: Isotopic and chemical signatures of high mountain
- 807 rivers in catchments with contrasting glacier and rock glacier cover, Journal of Hydrology, 623.
- 808 https://doi.org/10.1016/j.jhydrol.2023.129779, 2023.
- 809 Brighenti, S., Tolotti, M., Bruno, M. C., Engel, M., Wharton, G., Cerasino, L., Mair, V., and Bertoldi, W.: After the peak
- water: The increasing influence of rock glaciers on alpine river systems, Hydrological Processes, 33(21), 2804-2823,
- 811 https://doi.org/10.1002/hyp.13533, 2019.
- 812 Brunner, P., Therrien, R., Renard, P., Simmons, C. T., and Franssen, H.-J. H.: Advances in understanding river-groundwater
- 813 interactions, Reviews of Geophysics, 55(3), 818–854, https://doi.org/10.1002/2017RG000556, 2017.
- 814 Carrivick, J. L., and Heckmann, T.: Short-term geomorphological evolution of proglacial systems, Geomorphology, 287, 3-
- 815 28, <a href="https://doi.org/10.1016/j.geomorph.2017.01.037">https://doi.org/10.1016/j.geomorph.2017.01.037</a>, 2017.

# Field Code Changed

- 816 Carturan, L., Zuecco, G., Andreotti, A., Boaga, J., Morino, C., Pavoni, M., Seppi, R., Tolotti, M., Zanoner, T., and Zumiani,
- 817 M.: Spring-water temperature suggests widespread occurrence of Alpine permafrost in pseudo-relict rock glaciers, EGUsphere,
- 818 1–35, https://doi.org/10.5194/egusphere-2023-2689, 2024.
- Cartwright, I., and Hofmann, H.: Using radon to understand parafluvial flows and the changing locations of groundwater
  - inflows in the Avon River, southeast Australia, Hydrology and Earth System Sciences, 20(9), 3581-3600,
- 821 <u>https://doi.org/10.5194/hess-20-3581-2016</u>, 2016.
- 822 Casas-Mulet, R., Pander, J., Ryu, D., Stewardson, M. J., and Geist, J.: Unmanned Aerial Vehicle (UAV)-Based Thermal Infra-
- 823 Red (TIR) and Optical Imagery Reveals Multi-Spatial Scale Controls of Cold-Water Areas Over a Groundwater-Dominated
- 824 Riverscape, Frontiers in Environmental Science, 8, https://doi.org/10.3389/fenvs.2020.00064, 2020.
- 825 Chakravarti, P., Jain, V., and Mishra, V.: The distribution and hydrological significance of intact rock glaciers in the north-
- 826 west Himalaya, Geografiska Annaler, Series A: Physical Geography, 104(3), 226-244,
- 827 https://doi.org/10.1080/04353676.2022.2120262, 2022.
- 828 Charonnat, B. and Baraer, M.: Supplemental Material: Drone-Based Thermal Infrared Imagery for Detection of Cold
- 829 Groundwater Exfiltration in Shár Shaw Tagà, Yukon, Canada, Borealis, V1, https://doi.org/10.5683/SP3/O57OMY, 2025.
- 830 Chesnokova, A., Baraer, M., and Bouchard, É.: Proglacial icings as records of winter hydrological processes, The Cryosphere,
- 831 14(11), 4145–4164, <a href="https://doi.org/10.5194/tc-14-4145-2020">https://doi.org/10.5194/tc-14-4145-2020</a>, 2020.
- 832 Clow, D. W., Striegl, R. G., and Dornblaser, M. M.: Spatiotemporal Dynamics of CO2 Gas Exchange From Headwater
- Mountain Streams, Journal of Geophysical Research: Biogeosciences, 126(9), https://doi.org/10.1029/2021JG006509, 2021.
- Colombo, N., Ferronato, C., Vittori Antisari, L., Marziali, L., Salerno, F., Fratianni, S., D'Amico, M. E., Ribolini, A., Godone,
- 835 D., Sartini, S., Paro, L., Morra di Cella, U., and Freppaz, M.: A rock-glacier pond system (NW Italian Alps): Soil and
- sediment properties, geochemistry, and trace-metal bioavailability, Catena, 194, https://doi.org/10.1016/j.catena.2020.104700,
- 837 2020.

- 838 Colombo, N., Gruber, S., Martin, M., Malandrino, M., Magnani, A., Godone, D., Freppaz, M., Fratianni, S., and Salerno, F.:
- 839 Rainfall as primary driver of discharge and solute export from rock glaciers: The Col d'Olen Rock Glacier in the NW Italian
- 840 Alps, Science of the Total Environment, 639, 316–330, https://doi.org/10.1016/j.scitotenv.2018.05.098, 2018.
- Kaling Colombo, N., Salerno, F., Martin, M., Malandrino, M., Giardino, M., Serra, E., Godone, D., Said-Pullicino, D., Fratianni, S.,
- 842 Paro, L., Tartari, G., and Freppaz, M.: Influence of permafrost, rock and ice glaciers on chemistry of high-elevation ponds
- 843 (NW Italian Alps), Science of the Total Environment, 685, 886–901, https://doi.org/10.1016/j.scitotenv.2019.06.233, 2019.
- 644 Colucci, R. R., Forte, E., Žebre, M., Maset, E., Zanettini, C., and Guglielmin, M. Is that a relict rock glacier? Geomorphology,
- 330, 177–189, <a href="https://doi.org/10.1016/j.geomorph.2019.02.002">https://doi.org/10.1016/j.geomorph.2019.02.002</a>, 2019.
- 646 Croce, F., and Milana, J.: Internal structure and behavior of a Rock Glacier in the arid Andes of Argentina, Permafrost and
- Periglacial Processes, 13, 289–299, <a href="https://doi.org/10.1002/ppp.431">https://doi.org/10.1002/ppp.431</a>, 2002.

- Del Siro, C., Scapozza, C., Perga, M.-E., & Lambiel, C.: Investigating the origin of solutes in rock glacier springs in the Swiss
- Alps: A conceptual model, Frontiers in Earth Science, 11, <a href="https://doi.org/10.3389/feart.2023.1056305">https://doi.org/10.3389/feart.2023.1056305</a>, 2023.
- b50 Delaloye, R., Lambiel, C., and Gärtner-Roer, I.: Overview of rock glacier kinematics research in the Swiss Alps: Seasonal
- 851 rhythm, interannual variations and trends over several decades, Geographica Helvetica, 65(2), 135-145,
  - https://doi.org/10.5194/gh-65-135-2010, 2010.

868

879

- bodds, C.J., and Campbell, R.B.: Overview, legend and mineral deposit tabulations for: GSC Open File 2188 to Open File
- 2191, Geological Survey of Canada, Energy Mines and Resources Canada, 85 p. + 5 maps, 1992.
- Dugdale S. J.: A practitioner's guide to thermal infrared remote sensing of rivers and streams: recent advances, precautions
- and considerations, WIREs Water, vol. 3, no. 2, pp. 251–268, https://doi.org/10.1002/wat2.1135, 2016.
- 857 Engel, M., Penna, D., Bertoldi, G., Vignoli, G., Tirler, W., and Comiti, F.: Controls on spatial and temporal variability in
- streamflow and hydrochemistry in a glacierized catchment, Hydrology and Earth System Sciences, 23(4), 2041-2063,
- 859 <u>https://doi.org/10.5194/hess-23-2041-2019</u>, 2019.
- 860 Ensom, T., Makarieva, O., Morse, P., Kane, D., Alekseev, V., and Marsh, P.: The distribution and dynamics of aufeis in
- permafrost regions, Permafrost and Periglacial Processes, 31(3), 383–395, https://doi.org/10.1002/ppp.2051, 2020.
- 862 Evin, M., Fabre, D., and Johnson, P. G.: Electrical Resistivity Measurements on the Rock Glaciers of Grizzly Creek, St Elias
- Mountains, Yukon, Permafrost and Periglacial Processes, 8, 11, 1997.
- Falatkova, K., Šobr, M., Slavík, M., Bruthans, J., and Janský, B.: Hydrological characterization and connectivity of proglacial
- lakes to a stream, Adygine ice-debris complex, northern Tien Shan, Hydrological Sciences Journal, 65(4), 610-623,
- 866 https://doi.org/10.1080/02626667.2020.1711913, 2020.
- 867 Frauenfelder, R., Allgöwer, B., Haeberli, W., and Hoelzle, M.: Permafrost investigations with GIS a case study in the
  - Fletschhorn area, Wallis, SwissAlps, InPermafrost, Proceedings of the Seventh International Conference, 23-27June 1998,
- 869 Yellowknife, Canada, Lewkowicz AG, Allard M (eds) eds, Collection Nordicana 57, Centre d'études Nordiques, Université
- 870 Laval: Québec; 291-295, 1998.
- 871 Gammons, C. H., Doolittle, M. F., Eastman, K. A., and Poulson, S. R.: Geochemistry of natural acid rock drainage in the Mt
- 872 Evans area, Anaconda-Pintler Range, Montana, USA, Geochemistry: Exploration, Environment, Analysis, 21(4),
- https://doi.org/10.1144/geochem2021-068, 2021.
- 674 Gibson J.J., Holmes T., Stadnyk T.A., Birks S.J., Eby P., and Pietroniro A.: 180 and 2H in streamflow across Canada, Journal
- of Hydrology: Regional Studies, Volume 32, 100754, ISSN 2214-5818, https://doi.org/10.1016/j.eirh.2020.100754, 2020,
- 876 Haeberli, W.: Untersuchungen zur Verbreitung von Permafrost zwischen Flüelapass und Piz Grialetsch (Graubünden),
- Mitteilungen der VAW ETH Zürich 17: 1–221, 1975.
- Halla, C., Henrik Blöthe, J., Tapia Baldis, C., Trombotto Liaudat, D., Hilbich, C., Hauck, C., and Schrott, L.: Ice content and
  - interannual water storage changes of an active rock glacier in the dry Andes of Argentina, Cryosphere, 15(2), 1187-1213,
- 880 https://doi.org/10.5194/tc-15-1187-2021, 2021.

Formatted: Indent: Left: 0 cm, Border: Top: (No border) Bottom: (No border), Left: (No border), Right: (No border) Between: (No border)

Field Code Changed

Formatted: Indent: Left: 0 cm

Formatted: Indent: Left: 0 cm, Border: Top: (No border) Bottom: (No border), Left: (No border), Right: (No border) Between: (No border)

Formatted: Font color: Auto

- Harrington, J. S., Mozil, A., Hayashi, M., and Bentley, L. R.: Groundwater flow and storage processes in an inactive rock
- glacier, Hydrological Processes, 32(20), 3070–3088, <a href="https://doi.org/10.1002/hyp.13248">https://doi.org/10.1002/hyp.13248</a>, 2018.
- Harrison, S., Jones, D., Anderson, K., Shannon, S., and Betts, R. A.: Is ice in the Himalayas more resilient to climate change
- 884 than we thought? Geografiska Annaler, Series A: Physical Geography, 103(1), 1-7
- 885 https://doi.org/10.1080/04353676.2021.1888202, 2021.
- Hayashi, M.: Alpine Hydrogeology: The Critical Role of Groundwater in Sourcing the Headwaters of the World. Groundwater,
- 887 58(4), 498–510, <a href="https://doi.org/10.1111/gwat.12965">https://doi.org/10.1111/gwat.12965</a>, 2020.
- Hem, J. D.: Study and Interpretation of the Chemical Characteristics of Natural Water, 3rd Edition, US Geological Survey
- Water-Supply Paper 2254, University of Virginia, Charlottesville, 263 p., https://doi.org/10.3133/wsp2254, 1985,
- 890 Hewitt, K.: Rock Glaciers and Related Phenomena. In K. Hewitt (Ed.), Glaciers of the Karakoram Himalaya: Glacial
- 891 Environments, Processes, Hazards and Resources (pp. 267–289), Springer Netherlands, https://doi.org/10.1007/978-94-007-
- 892 6311-1 11, 2014.
- Hock, R., Rasul, G., Adler, C., Cáceres, B., Gruber, S., Hirabayashi, Y., Jackson, M., Kääb, A., Kang, S., Kutuzov, S., Milner,
- 894 Al., Molau, U., Morin, S., Orlove, B., and Steltzer, H.: High Mountain Areas. In: IPCC Special Report on the Ocean and
- 895 Cryosphere in a Changing Climate [Pörtner, H.-O., Roberts, D.C., Masson-Delmotte, V., Zhai, P., Tignor, M., Poloczanska,
- 896 E., Mintenbeck, K., Alegría, A., Nicolai, M., Okem, A., Petzold, J., Rama, B. and Weyer N.M. (eds.)]: Cambridge University
- 897 Press, Cambridge, UK and New York, NY, USA, pp. 131-202, https://doi.org/10.1017/9781009157964.004, 2019.
- 898 Hu, X., and Pollard, W.H.: The hydrologic analysis and modelling of river icing growth, North Fork Pass, Yukon Territory,
- 899 Canada, Permafrost and Periglacial Processes, 8: 279–294, https://doi.org/10.1002/(SICI)1099-1530(199709)8:3<279::AID-
- 900 PPP260>3.0.CO;2-7, 1997,
- 901 Huss, M., Bookhagen, B., Huggel, C., Jacobsen, D., Bradley, R. S., Clague, J. J., Vuille, M., Buytaert, W., Cayan, D. r.,
- 902 Greenwood, G., Mark, B. g., Milner, A. M., Weingartner, R., and Winder, M.: Toward mountains without permanent snow
- and ice, Earth's Future, 5(5), 418–435, <a href="https://doi.org/10.1002/2016EF000514">https://doi.org/10.1002/2016EF000514</a>, 2017.
- 904 Iwasaki, K., Fukushima, K., Nagasaka, Y., Ishiyama, N., Sakai, M., and Nagasaka, A.: Real-Time Monitoring and
- 905 Postprocessing of Thermal Infrared Video Images for Sampling and Mapping Groundwater Discharge, Water Resources
- 906 Research, 59(4), e2022WR033630, https://doi.org/10.1029/2022WR033630, 2023.
- 907 Iwasaki, K., Nagasaka Y., Ishiyama N., and Nagasaka A.: Thermal imaging survey for characterizing bedrock groundwater
- 908 discharge: comparison between sedimentary and volcanic catchments, Hydrological Research Letters 18(3): 79-86,
- 909 http://dx.doi.org/10.3178/hrl.18.79, 2024,
- 910 Johnson, P. G.: Holocene Paleohydrology of the St. Elias Mountains, British Columbia and Yukon, Géographie Physique et
- 911 Quaternaire, 40(1), 47–53, <a href="https://doi.org/10.7202/032622ar">https://doi.org/10.7202/032622ar</a>, 1986.
- p12 Johnson, P. G.: Mass Movement of Ablation Complexes and Their Relationship to Rock Glaciers, Geografiska Annaler, Series
- 913 A, Physical Geography, 56(1/2), 93–101, <a href="https://doi.org/10.2307/520430">https://doi.org/10.2307/520430</a>, 1974.

Formatted: Indent: Left: 0 cm, Border: Top: (No border) Bottom: (No border), Left: (No border), Right: (No border) Between: (No border)

Formatted: Font color: Auto

Formatted: Indent: Left: 0 cm

Formatted: Indent: Left: 0 cm, Border: Top: (No border) Bottom: (No border), Left: (No border), Right: (No border) Between: (No border)

Formatted: Font color: Auto

Formatted: Indent: Left: 0 cm

Formatted: Indent: Left: 0 cm, Border: Top: (No border) Bottom: (No border), Left: (No border), Right: (No border) Between: (No border)

Formatted: Font color: Auto, English (United States)

- 914 Johnson, P. G.: Rock glacier types and their drainage systems, Grizzly Creek, Yukon Territory, Canadian Journal of Earth
- 915 Sciences, 15(9), 1496–1507, https://doi.org/10.1139/e78-155, 1978.
- 916 Johnson, P. G.: Glacier-Rock Glacier Transition in the Southwest Yukon Territory, Canada, Arctic and Alpine Research, 12(2),
- 917 195, https://doi.org/10.2307/1550516, 1980.
- 918 Johnson, P. G.: Rock Glaciers, A Case for a Change in Nomenclature, Geografiska Annaler, Series A, Physical Geography,
- 919 65(1/2), 27–34, https://doi.org/10.2307/520718, 1983.
- p20 Johnson, P. G.: Stagnant Glacier Ice, St. Elias Mountains, Yukon, Geografiska Annaler, Series A, Physical Geography, 74(1),
- 921 13–19, <a href="https://doi.org/10.2307/521466">https://doi.org/10.2307/521466</a>, 1992.
- 922 Jones, D. B., Harrison, S., Anderson, K., and Betts, R. A.: Mountain rock glaciers contain globally significant water stores,
- 923 Scientific Reports, 8(1), Article 1, https://doi.org/10.1038/s41598-018-21244-w, 2018.
- 924 Jones, D. B., Harrison, S., Anderson, K., Shannon, S., and Betts, R. A.: Rock glaciers represent hidden water stores in the
- 925 Himalaya, Science of The Total Environment, 793, 145368, https://doi.org/10.1016/j.scitotenv.2021.145368, 2021.
- Jones, D. B., Harrison, S., Anderson, K., and Whalley, W. B.: Rock glaciers and mountain hydrology: A review, Earth-Science
- 927 Reviews, 193, 66–90, <a href="https://doi.org/10.1016/j.earscirev.2019.04.001">https://doi.org/10.1016/j.earscirev.2019.04.001</a>, 2019.
- 928 Kalbus, E., Reinstorf, F., and Schirmer, M.: Measuring methods for groundwater and surface water interactions: review,
- 929 Hydrology and Earth System Sciences, 10(6), 873–887, <a href="https://doi.org/10.5194/hess-10-87">https://doi.org/10.5194/hess-10-87</a>3-2006, 2006.
- Water Resources Käser, D., and Hunkeler, D.: Contribution of alluvial groundwater to the outflow of mountainous catchments. Water Resources
- 931 Research, 52(2), 680–697, https://doi.org/10.1002/2014WR016730, 2016.
- 932 Krainer, K., and Mostler, W.: Hydrology of Active Rock Glaciers: Examples from the Austrian Alps, Arctic, Antarctic, and
- 933 Alpine Research, 34(2), 142–149, https://doi.org/10.1080/15230430.2002.12003478, 2002.
- 934 Krainer, K., Mostler, W., and Spötl, C.: Discharge from active rock glaciers, Austrian Alps: A stable isotope approach, Austrian
- 935 Journal of Earth Sciences, 100, 102–112, 2007.
- 936 Kummert, M., Bodin, X., Braillard, L., and Delaloye, R.: Pluri-decadal evolution of rock glaciers surface velocity and its
- 937 impact on sediment export rates towards high alpine torrents, Earth Surface Processes and Landforms, 46(15), 3213-3227,
- 938 https://doi.org/10.1002/esp.5231, 2021.
- 939 Liu, W., Fortier, R., Molson, J., and Lemieux, J.: A conceptual model for talik dynamics and icing formation in a river
- 940 floodplain in the continuous permafrost zone at Salluit, Nunavik (Quebec), Canada, Permafrost and Periglacial Processes,
- 941 32(3), 468–483, https://doi.org/10.1002/ppp.2111, 2021.
- b42 Lloyd, S.: Least squares quantization in PCM, IEEE Transactions on Information Theory, 28(2), 129-137, IEEE Transactions
- on Information Theory, <a href="https://doi.org/10.1109/TIT.1982.1056489">https://doi.org/10.1109/TIT.1982.1056489</a>, 1982.
- MacQueen, J.: Some methods for classification and analysis of multivariate observations, In Proceedings of the fifth Berkeley
- symposium on mathematical statistics and probability (Vol. 1, No. 14, pp. 281-297), 1967.

- 946 Mallinson, L., Swift, D. A., and Sole, A.: Proglacial icings as indicators of glacier thermal regime: Ice thickness changes and
- 947 icing occurrence in Svalbard, Geografiska Annaler, Series A. Physical Geography, 101(4), 334-349,
- 948 <a href="https://doi.org/10.1080/04353676.2019.1670952">https://doi.org/10.1080/04353676.2019.1670952</a>, 2019.
- Marcer, M., Cicoira, A., Cusicanqui, D., Bodin, X., Echelard, T., Obregon, R., and Schoeneich, P.: Rock glaciers throughout
- 950 the French Alps accelerated and destabilised since 1990 as air temperatures increased, Communications Earth & Environment,
- 951 2(1), 1–11, <a href="https://doi.org/10.1038/s43247-021-00150-6">https://doi.org/10.1038/s43247-021-00150-6</a>, 2021.
- 952 Marren, P. M., and Toomath, S. C.: Channel pattern of proglacial rivers: Topographic forcing due to glacier retreat, Earth
- 953 Surface Processes and Landforms, 39(7), 943–951, https://doi.org/10.1002/esp.3545, 2014.
- 954 Müller, T., Lane, S. N., and Schaefli, B.: Towards a hydrogeomorphological understanding of proglacial catchments: An
- assessment of groundwater storage and release in an Alpine catchment, Hydrology and Earth System Sciences, 26(23), 6029-
- 956 6054, <a href="https://doi.org/10.5194/hess-26-6029-2022">https://doi.org/10.5194/hess-26-6029-2022</a>, 2022.
- 957 Müller, T., Roncoroni, M., Mancini, D., Lane, S. N., and Schaefli, B.: Current and future roles of meltwater-groundwater
- 958 dynamics in a proglacial Alpine outwash plain, Hydrology and Earth System Sciences, 28(4), 735-759,
- 959 <u>https://doi.org/10.5194/hess-28-735-2024, 2024.</u>
- 960 Navarro, G., Valois, R., MacDonell, S., de Pasquale, G., and Díaz, J. P.: Internal structure and water routing of an ice-debris
- 961 landform assemblage using multiple geophysical methods in the semiarid Andes, Frontiers in Earth Science, 11,
- 962 https://doi.org/10.3389/feart.2023.1102620, 2023.
- 963 PERMOS Report 2019-16-19 | PERMOS Swiss Permafrost Monitorinig Network, Retrieved 17 September 2024, from
- 964 https://www.permos.ch/doi/permos-rep-2019-16-19, 2019.
- Poster, C., Howat, I., Noh, M.-J., Husby, E., Khuvis, S., Danish, E., Tomko, K., Gardiner, J., Negrete, A., Yadav, B., Klassen,
- 966 J., Kelleher, C., Cloutier, M., Bakker, J., Enos, J., Arnold, G., Bauer, G., and Morin, P.: ArcticDEM Mosaics, Version 4.1
- 967 [Dataset], Harvard Dataverse, <a href="https://doi.org/10.7910/DVN/3VDC4W">https://doi.org/10.7910/DVN/3VDC4W</a>, 2023.
- 968 Rautio, A., Kivimäki, A.-L., Korkka-Niemi, K., Nygård, M., Salonen, V.-P., Lahti, K., and Vahtera, H.: Vulnerability of
- 969 groundwater resources to interaction with river water in a boreal catchment, Hydrology and Earth System Sciences, 19(7),
- 970 3015–3032, https://doi.org/10.5194/hess-19-3015-2015, 2015.
- P71 Reato, A., Borzi, G., Martínez, O. A., and Carol, E.: Role of rock glaciers and other high-altitude depositional units in the
- 972 hydrology of the mountain watersheds of the Northern Patagonian Andes, Science of The Total Environment, 824, 153968,
- 973 https://doi.org/10.1016/j.scitotenv.2022.153968, 2022.
- 974 Robinson, C. T., Jolidon, C., Consoli, G., Bloem, S., and Ebi, C.: Temporal dynamics in the physico-chemistry of a high-
- alpine stream network in the Swiss National Park, Eco.Mont, 14(2), 11-23, https://doi.org/10.1553/eco.mont-14-2s11, 2022.
- 976 Scapozza, C.: Contributo dei metodi termici alla prospezione del permafrost montano: esempi dal massiccio della Cima di
- 977 Gana Bianca (Val Blenio, Svizzera), Bollettino della Società Ticinese di Scienze Naturali 97:55-66, 2009.

- 978 Scapozza, C.: Investigation on protalus ramparts in the Swiss Alps, Geographica Helvetica, 70(2), 135-139,
- 979 <u>https://doi.org/10.5194/gh-70-135-2015</u>, 2015.
- 980 Schreder, S., Sommaruga, R., Psenner, R., Chimani, B., Ganekind, M., and Koinig, K. A.: Changes in air temperature, but not
- 981 in precipitation, determine long-term trends in water chemistry of high mountain lakes of the Alps with and without rock
- 982 glacier influence, Science of the Total Environment, 905, https://doi.org/10.1016/j.scitotenv.2023.167750, 2023.
- 983 Scotti, R., Crosta, G. B., and Villa, A.: Destabilisation of Creeping Permafrost: The Plator Rock Glacier Case Study (Central
- Italian Alps), Permafrost and Periglacial Processes, 28(1), 224–236, https://doi.org/10.1002/ppp.1917, 2017.
- 985 Sorg, A., Kääb, A., Roesch, A., Bigler, C., and Stoffel, M.: Contrasting responses of Central Asian rock glaciers to global
- warming, Scientific Reports, 5, https://doi.org/10.1038/srep08228, 2015.
- P87 Terry, N., Grunewald, E., Briggs, M., Gooseff, M., Huryn, A. D., Kass, M. A., Tape, K. D., Hendrickson, P., and Lane, J. W.,
- 988 Jr.: Seasonal Subsurface Thaw Dynamics of an Aufeis Feature Inferred From Geophysical Methods, Journal of Geophysical
- 989 Research: Earth Surface, 125(3), https://doi.org/10.1029/2019JF005345, 2020.
- 990 Tjoelker, A., Baraer, M., Valence, E., Charonnat, B., Masse-Dufresne, J., Mark, B., and McKenzie, J.: Drone-Based Ground-
- 991 Penetrating Radar with Manual Transects for Improved Field Surveys of Buried Ice, Remote Sensing, 16, 2461,
- 992 <u>https://doi.org/10.3390/rs16132461</u>, 2024.
- 993 Toran, L.: Groundwater-Surface Water Interaction, In Encyclopedia of Water (pp. 1-12), John Wiley & Sons, Ltd,
- 994 https://doi.org/10.1002/9781119300762.wsts0027, 2019.
- 795 Torgersen C. E., Faux R. N., McIntosh B. A., Poage N. J., and Norton D. J.: Airborne thermal remote sensing for water
- temperature assessment in rivers and streams, Remote Sensing of Environment, vol. 76, no. 3, pp. 386-398,
- 997 https://doi.org/10.1016/S0034-4257(01)00186-9, 2001,
- 998 Tronstad, L. M., Hotaling, S., Giersch, J. J., Wilmot, O. J., and Finn, D. S.: Headwaters Fed by Subterranean Ice: Potential
- 999 Climate Refugia for Mountain Stream Communities? Western North American Naturalist, 80(3), 395-407,
- 1000 https://doi.org/10.3398/064.080.0311, 2020.

- 1001 van Tiel, M., Aubry-Wake, C., Somers, L., Andermann, C., Avanzi, F., Baraer, M., Chiogna, G., Daigre, C., Das, S., Drenkhan,
- 1002 F., Farinotti, D., Fyffe, C. L., de Graaf, I., Hanus, S., Immerzeel, W., Koch, F., McKenzie, J. M., Müller, T., Popp, A. L., ...
- 1003 Yapiyev, V.: Cryosphere–groundwater connectivity is a missing link in the mountain water cycle, Nature Water, 2(7), 624–
- 1004 637, https://doi.org/10.1038/s44221-024-00277-8, 2024.
- 1005 Vélez-Nicolás, M., García-López, S., Barbero, L., Ruiz-Ortiz, V., and Sánchez-Bellón, Á.: Applications of Unmanned Aerial
  - Systems (UASs) in Hydrology: A Review, Remote Sensing, 13(7), Article 7, https://doi.org/10.3390/rs13071359, 2021.
- 1007 Wagner, T., Brodacz, A., Krainer, K., and Winkler, G.: Active rock glaciers as shallow groundwater reservoirs, Austrian Alps,
- 1008 Grundwasser, 25(3), 215–230, https://doi.org/10.1007/s00767-020-00455-x, 2020.
- 1009 Wagner, T., Kainz, S., Krainer, K., and Winkler, G.: Storage-discharge characteristics of an active rock glacier catchment in
- the Innere Ölgrube, Austrian Alps, Hydrological Processes, 35(5), <a href="https://doi.org/10.1002/hyp.14210">https://doi.org/10.1002/hyp.14210</a>, 2021.

Formatted: Indent: Left: 0 cm, Border: Top: (No border) Bottom: (No border), Left: (No border), Right: (No border) Between: (No border)

Formatted: Font color: Auto

- 1011 Wagner, T., Pauritsch, M., and Winkler, G.: Impact of relict rock glaciers on spring and stream flow of alpine watersheds:
- 1012 Examples of the Niedere Tauern Range, Eastern Alps (Austria), Austrian Journal of Earth Sciences, 109(1),
- 1013 https://doi.org/10.17738/ajes.2016.0006, 2016.
- 1014 Wahl, H. E., Fraser, D. B., Harvey, R. C., and Maxwell, J. B.: Climate of Yukon, Atmospheric Environment Service,
- 1015 Environment Canada, 1987,
- 1016 Wainstein, P., Moorman, B., and Whitehead, K.: Glacial conditions that contribute to the regeneration of Fountain Glacier
- proglacial icing, Bylot Island, Canada, Hydrological Processes, 28(5), 2749–2760, https://doi.org/10.1002/hyp.9787, 2014.
  - Wanner, C., Moradi, H., Ingold, P., Cardenas Bocanegra, M. A., Mercurio, R., and Furrer, G.: Rock glaciers in the Central
- 1019 Eastern Alps How permafrost degradation can cause acid rock drainage, mobilization of toxic elements and formation of
  - basaluminite, Global and Planetary Change, 227, https://doi.org/10.1016/j.gloplacha.2023.104180, 2023.
- 1021 Webb, B. W., Hannah, D. M., Moore, R. D., Brown, L. E., and Nobilis, F.: Recent advances in stream and river temperature
- 1022 research, Hydrological Processes, 22(7), 902–918, https://doi.org/10.1002/hyp.6994, 2008.
- 1023 Winkler, G., Wagner, T., Pauritsch, M., and Kellerer-Pirklbauer, A.: What will occur after permafrost? Relevance of relict
  - rock glaciers for the discharge behaviour of alpine catchments, Joannea Geologie und Palaontologie, 12, 63–72, 2016.
- 1025 Zappa C. J., Jessup A. T., and Yeh H.: Skin layer recovery of free-surface wakes: Relationship to surface renewal and
- dependence on heat flux and background turbulence, Journal of Geophysical Research: Oceans, vol. 103, no. C10, pp. 21711—
- 1027 21722, 1998, https://doi.org/10.1029/98JC01942, 1998,
- 1028 Zarroca, M., Roqué, C., Linares, R., Salminci, J. G., and Gutiérrez, F.: Natural acid rock drainage in alpine catchments: A side
- effect of climate warming, Science of The Total Environment, 778, 146070, https://doi.org/10.1016/j.scitotenv.2021.146070,
- 1030 2021.

1020

1024

- 1031 Zierl, B., and Bugmann, H.: Global change impacts on hydrological processes in Alpine catchments, Water Resources
- 1032 Research, 41(2), https://doi.org/10.1029/2004WR003447, 2005.

Formatted: Indent: Left: 0 cm, Border: Top: (No border) Bottom: (No border), Left: (No border), Right: (No border) Between: (No border)

Formatted: Font color: Auto

Formatted: Indent: Left: 0 cm

Formatted: Indent: Left: 0 cm, Border: Top: (No border) Bottom: (No border), Left: (No border), Right: (No border) Between: (No border)

Formatted: Font color: Auto